



DIGITAL ACCESS TO  
SCHOLARSHIP AT HARVARD  
DASH.HARVARD.EDU



HARVARD LIBRARY  
Office for Scholarly Communication

# Phosphorus sources for phosphatic Cambrian carbonates

The Harvard community has made this  
article openly available. [Please share](#) how  
this access benefits you. Your story matters

Citation	Creveling, J. R., D. T. Johnston, S. W. Poulton, B. Kotrc, C. Marz, D. P. Schrag, and A. H. Knoll. 2013. "Phosphorus Sources for Phosphatic Cambrian Carbonates." <i>Geological Society of America Bulletin</i> 126 (1-2) (December 6): 145–163. doi:10.1130/b30819.1.
Published Version	doi:10.1130/B30819.1
Citable link	<a href="http://nrs.harvard.edu/urn-3:HUL.InstRepos:16422963">http://nrs.harvard.edu/urn-3:HUL.InstRepos:16422963</a>
Terms of Use	This article was downloaded from Harvard University's DASH repository, and is made available under the terms and conditions applicable to Open Access Policy Articles, as set forth at <a href="http://nrs.harvard.edu/urn-3:HUL.InstRepos:dash.current.terms-of-use#OAP">http://nrs.harvard.edu/urn-3:HUL.InstRepos:dash.current.terms-of-use#OAP</a>

1 **P sources for phosphatic Cambrian carbonates**

2 Jessica R. Creveling<sup>1\*</sup>, David T. Johnston<sup>1†</sup>, Simon W. Poulton<sup>2</sup>, Benjamin Kotrc<sup>1</sup>,  
3 Christian März<sup>3</sup>, Daniel P. Schrag<sup>1</sup>, Andrew H. Knoll<sup>1,4</sup>

4 <sup>1</sup> *Department of Earth and Planetary Sciences, Harvard University, 20 Oxford Street,*  
5 *Cambridge, MA 02138, USA*

6 <sup>2</sup> *School of Earth and Environment, University of Leeds, Leeds, LS2 9JT, UK*

7 <sup>3</sup> *School of Civil Engineering and Geosciences, Newcastle University, Drummond*  
8 *Building, Newcastle upon Tyne, NE1 7RU, UK*

9 <sup>4</sup> *Department of Organismic and Evolutionary Biology, Harvard University, 26 Oxford*  
10 *Street, Cambridge, MA 02138, USA*

11 \*Email: [jcrevel@gps.caltech.edu](mailto:jcrevel@gps.caltech.edu)

12 †Email: [johnston@eps.harvard.edu](mailto:johnston@eps.harvard.edu)

13

14 **ABSTRACT**

15 **The fossilization of organic remains and shell material by calcium phosphate**  
16 **minerals provides an illuminating, but time-bounded, window into Ediacaran—**  
17 **Cambrian animal evolution. For reasons that remain unknown, phosphatic fossil**  
18 **preservation declined significantly through Cambrian Series 2. Here we investigate**  
19 **the phosphorus (P) sources for phosphatic Cambrian carbonates, presenting**  
20 **sedimentological, petrographic, and geochemical data from the Cambrian Series 2–**  
21 **3 Thornton Limestone, Australia, some of the youngest Cambrian strata to display**  
22 **exceptional phosphatic preservation of small shelly fossils. We find that within**  
23 **Thornton sediments, phosphate was remobilized by organic decay and bacterial**  
24 **iron reduction, with subsequent reprecipitation largely as apatite within the**  
25 **interiors of small shelly fossils. We discuss the merits of bioclastic-derived, organic**  
26 **matter-bound, or iron-bound P as potential sources to these strata. Petrographic**  
27 **observations suggest that the dissolution of phosphatic skeletal material did not**  
28 **source P for fossil preservation. In contrast, high organic carbon contents imply**  
29 **significant organic fluxes of P to Thornton sediments. Sedimentology and iron-**  
30 **speciation data indicate that phosphorus enrichment occurred during times of**  
31 **expanded anoxic, ferruginous conditions in subsurface water masses, suggesting**  
32 **that phosphorus adsorption to iron minerals precipitating from the water column**  
33 **provided a second significant P source to Thornton sediments. Simple**

34 **stoichiometric models suggest that by themselves neither organic carbon burial nor**  
35 **an iron shuttle can account for the observed phosphorus enrichment. Thus, we infer**  
36 **that both processes were necessary for the observed phosphorus enrichment and**  
37 **subsequent fossil preservation in the Thornton Limestone.**

38

## 39 INTRODUCTION

40 Phosphorite and phosphatic carbonate define a spectrum of sedimentary lithologies  
41 enriched in the authigenic calcium phosphate mineral apatite (Kazakov, 1937; Baturin  
42 and Bezrukov, 1979; Riggs, 1986; Cook and Shergold, 1986; Cook et al., 1990; Föllmi,  
43 1996; Trappe, 2001). The punctuated temporal distribution (Cook and McElhinny, 1979;  
44 Cook and Shergold, 1984, 1986) and evolving spatial distribution (Brasier and Callow,  
45 2007) of phosphatic lithologies through Earth history suggest that unique and restrictive  
46 physical (Filippelli and Delaney, 1992) and/or chemical (e.g., Föllmi, 1996) conditions  
47 govern phosphate deposition in time and space.

48         There are many reasons to want to understand this distribution. Perhaps foremost  
49 is the practical concern for understanding how ore-grade sedimentary phosphorites form  
50 (e.g., Cook and Shergold, 1986). As with petroleum, phosphate ores are approaching  
51 peak production, while global demand continues to rise (Cordell et al., 2009; Filippelli,  
52 2011). At the same time, biogeochemists increasingly invoke perturbations to the ancient  
53 phosphorus cycle to explain inferred fluctuations in biological productivity, organic  
54 carbon burial and oxidant accumulation over geological time-scales (Tyrrell, 1999;  
55 Bjerrum and Canfield, 2002; Saltzman, 2005; Holland et al., 2006; Konhauser et al.,  
56 2007; Algeo and Ingall, 2007; Planavsky et al., 2010; Swanson-Hysell et al., 2012).  
57 Finally, phosphatic deposits provide a direct window into evolutionary history through

58 the exceptional preservation of fossils (Cook, 1992; Bengtson and Zhao, 1997; Xiao and  
59 Knoll, 2000; Butterfield, 2003; Porter, 2004a).

60 A global phosphogenic window coincides with major evolutionary innovation  
61 during the Ediacaran and Cambrian periods (Cook and Shergold, 1984; 1986; Cook,  
62 1992). Much of our knowledge of early animal diversification derives from  
63 biomineralized and soft-bodied metazoans replaced and/or templated by phosphate  
64 minerals (Bengtson et al., 1990; Xiao and Knoll, 1999; 2000; Donoghue et al., 2006;  
65 Dornbos et al., 2006; Kouchinsky et al., 2012). Phosphatization taphonomy is tied to the  
66 biogeochemical cycle of phosphorus and, for reasons that remain unknown, a major  
67 decline in the incidence of phosphatic lithologies and phosphatic fossil preservation  
68 occurs during Cambrian Series 2 (Cook and McElhinny, 1979; Porter, 2004b; Donoghue  
69 et al., 2006). To understand the loss of phosphatic lithologies, and the consequent closure  
70 of the Cambrian phosphatization taphonomic window, we must first understand how  
71 phosphorus entered the sediment column and how it was subsequently redistributed and  
72 concentrated around skeletal elements. In this paper, we ask specifically: what was the  
73 source of phosphorus to phosphatic carbonates characterized by exceptional skeletal  
74 preservation?

75 Geochemistry provides one avenue to address this question. A common view  
76 holds that enhanced delivery of reactive phosphorus (i.e., phosphorus that may undergo  
77 biogeochemical transformations within the sediment column) to the sea floor is the  
78 primary variable governing the development of phosphatic lithologies (e.g., see Föllmi,  
79 1996, and references therein; Papineau, 2010). In modern marine environments, the  
80 delivery of reactive phosphorus to the sea floor occurs predominantly in association with

81 two phases (e.g., Delaney, 1998; Benitez-Nelson, 2000): phosphorus bound within  
82 organic matter (Redfield, 1958) and/or phosphorus adsorbed to/co-precipitated with  
83 particulate iron minerals (herein referred to as the ‘Fe-P shuttle’) (Berner, 1973; Shaffer,  
84 1986; Feely et al., 1991; Feely et al., 1998; Poulton and Canfield, 2006). To examine the  
85 extent to which these reactive phosphorus sources contributed to ancient phosphatic  
86 deposits, we report high-resolution phosphorus and iron speciation data, stable carbon  
87 isotope measurements, and trace element concentrations for the phosphatic Thornton  
88 Limestone, Georgina Basin, Australia (Cambrian Series 2–3; Southgate, 1988; Southgate  
89 and Shergold, 1991), and, for comparison, the overlying non-phosphatic Arthur Creek  
90 Formation. We explore the possibility that bioclastic-bound, organic-bound, and iron-  
91 bound P sourced the Thornton phosphatic carbonates and develop simple mathematical  
92 models to assess the relative importance of organic- and iron-bound P. We find that while  
93 the high organic carbon content of the Thornton Limestone suggests that organic-bound  
94 P contributed significantly to authigenic apatite formation, C to P ratios indicate that  
95 organic-bound P was insufficient to account entirely for the observed phosphorus  
96 enrichment. Sedimentology and iron speciation data indicate that these formations  
97 accumulated under anoxic, ferruginous subsurface water masses, allowing for the  
98 possibility that P adsorbed to iron minerals precipitating from the water column  
99 augmented organic-bound P delivery to the sediment column. Nonetheless, simple  
100 mathematical models indicate that, by itself, iron-bound phosphorus delivery is also  
101 incapable of accounting for the observed phosphorus enrichment. Thus, we infer that both  
102 organic-bound and iron-bound phosphorus sources were necessary for the development  
103 of the fossil-bearing phosphatic carbonates of the Thornton Limestone.

104

105 **GEOLOGIC BACKGROUND**

106 The Centralian Superbasin is a laterally extensive intracratonic basin that initiated during  
107 Neoproterozoic transcontinental rifting of Rodinia. Regional tectonic events subsequently  
108 dissected the superbasin into a mosaic of discrete, asymmetric, polyphase foreland basins  
109 (Fig. 1a; Walter et al, 1995; Lindsay, 2002; Dunster et al., 2007). Here, we focus on the  
110 phosphatic Cambrian strata of the southern Georgina Basin (Cook and Shergold, 1986;  
111 Southgate, 1988; Southgate and Shergold, 1991), which deposited variably and  
112 diachronously across the basin (Cook and Shergold, 1986; Southgate, 1988; Howard,  
113 1990; Southgate and Shergold, 1991; Dunster et al., 2007).

114 The Narpa Group encompasses Cambrian Series 2 and Series 3 stratigraphy of the  
115 southern Georgina Basin (Fig. 1b; Ambrose et al., 2001; Dunster et al., 2007). Deposition  
116 of its lowermost member, the phosphatic Thornton Limestone, reflects a major  
117 transgression and expansion of the Georgina Basin. For this reason, the basal contact of  
118 the Thornton Limestone can unconformably overlie the Shadow Group, conformably  
119 and gradationally overlie the Shadow Group, or overlie and re-work crystalline basement  
120 (Fig. 1b). The rest of the Narpa Group records a basin-wide, shallowing-upward  
121 succession that transitions from outer (lower Arthur Creek Formation), middle (upper  
122 Arthur Creek Formation) and inner ramp (Steamboat Sandstone) depositional  
123 environments into a flat-topped carbonate platform (Arrintheta Formation; Ambrose et  
124 al., 2001; Dunster et al., 2007).

125 Trilobite biostratigraphy assigns Thornton rocks to the Ordian and early  
126 Templetonian stages of Australian chronostratigraphy (Laurie, 2004a,b; Dunster et al.,

127 2007), correlative to Cambrian Series 2, Stage 4 and, possibly, lowermost Series 3, Stage  
128 5 (Fig. 1b; Babcock and Peng, 2007; Peng and Babcock, 2011). Trilobite biozones within  
129 the Arthur Creek Formation are diagnostic for the Australian regional Ordian–  
130 Boomerangian stages (Laurie, 2004a, b; Dunster et al., 2007), correlative to uppermost  
131 Stage 4 of Cambrian Series 2 through to the Guzhangian Stage of Cambrian Series 3 (Fig.  
132 1b; Babcock and Peng, 2007; Peng and Babcock, 2011).

133

## 134 **METHODS**

135 We examined the sedimentology and lithofacies associations of the Thornton and  
136 Arthur Creek formations within drill core NTGS 99/1 repositied at the Northern Territory  
137 Geological Survey, Alice Springs, Australia. With a water-cooled saw, we cut 534 three-  
138 cm-long, quarter-core samples perpendicular to bedding at ~10-25 cm resolution between  
139 597.58 and 347.98 meters core depth (mcd). Each sample was again divided  
140 (perpendicular to bedding) into two subsamples, one half designated as a hand-sample or  
141 thin-section billet, the other half pulverized with a steel ring mill. Each hand-sample  
142 billet was micro-drilled along individual laminations for carbonate carbon ( $\delta^{13}\text{C}_{\text{carb}}$ ) and  
143 carbonate oxygen ( $\delta^{18}\text{O}_{\text{carb}}$ ) isotopic analysis. The evolved  $\text{CO}_2$  was measured against an  
144 in-house reference gas on a VG Optima dual-inlet mass spectrometer attached to a VG  
145 Isocarb preparation system. We report isotopic values in the V-PDB per mil (‰)  
146 notation. Standard reproducibility was  $1\sigma = < 0.1\text{‰}$  and  $0.2\text{‰}$  for  $\delta^{13}\text{C}_{\text{carb}}$  and  $\delta^{18}\text{O}_{\text{carb}}$ ,  
147 respectively.

148 Sample powders were divided for carbon, phosphorus, iron, and trace element  
149 geochemical analyses aimed at diagnosing the sediment- and water-column geochemistry

150 at the time of phosphatic carbonate deposition. To determine carbon mass fractions, we  
151 acidified 5-10 g of powdered sample with cold, 2.5 M hydrochloric acid. The resulting  
152 insoluble residue (i.e., the non-carbonate fraction, comprised predominately of  
153 siliciclastics and organic matter) was isolated by filtration, rinsed thoroughly with de-  
154 ionized water, then dried and weighed. The total carbonate fraction was estimated as the  
155 weight percent difference between the bulk sample and the insoluble residue. To  
156 determine the weight percent of total organic carbon (TOC) and its isotopic composition  
157 ( $\delta^{13}\text{C}_{\text{org}}$ ), aliquots of the insoluble residue were combusted within a Carlo Erba NA 1500  
158 Analyzer attached to a Thermo Scientific Delta V Advantage isotope ratio mass  
159 spectrometer. Reproducibility of  $\delta^{13}\text{C}_{\text{org}}$  for an acetanilide standard was 0.16‰ ( $1\sigma$ ). Of  
160 the 100 samples processed, 29 were analyzed in duplicate and yielded an analytical  
161 reproducibility of  $1\sigma = 0.07$  weight percent (wt.%) TOC. Finally, we estimated the wt.%  
162 of silicate phases (either clastic or authigenic) as the wt.% of the insoluble fraction minus  
163 the wt.% of the TOC fraction.

164 The speciation of phosphorus (P) was determined with a modified sequential  
165 extraction methodology for marine sediment (Ruttenberg, 1992). Here, 150-200 mg of  
166 rock powder was sequentially extracted with 10 mL each of (1) 0.3 M sodium-citrate/1 M  
167 sodium bicarbonate/0.14 M sodium dithionite (pH = 7.5) for P bound to  
168 reducible/reactive ferric iron minerals ( $\text{P}_{\text{Fe}}$ ), (2) 1 M sodium acetate (pH = 4.0) for  
169 carbonate fluorapatite, biogenic hydroxyapatite, and carbonate-bound P ( $\text{P}_{\text{auth+carb}}$ ), (3) 1.2  
170 M cold HCl for crystalline fluorapatite ( $\text{P}_{\text{x1}}$ ), and (4) 1.2 M cold HCl after a 2 hour  
171 ignition at 550°C for organic P ( $\text{P}_{\text{org}}$ ). To prevent P readsorption during the first two  
172 extraction steps, two 5 mL 1 M  $\text{MgCl}_2$  washes were performed post-extraction.



173 Phosphorus in extracts and wash solutions (except  $P_{Fe}$ ) was analyzed  
174 spectrophotometrically (Thermo Genesys 6) by the molybdate-blue method (Strickland  
175 and Parsons, 1972; Ruttenberg, 1992);  $P_{Fe}$  was measured by inductively coupled plasma  
176 optical emission spectrometry (ICP-OES; Varian Vista-MPX). We note that Ruttenberg  
177 (1992) ascribes P-speciation phase (3),  $P_{xl}$ , to detrital fluorapatite of igneous and  
178 metamorphic origin. We abbreviate this phase as 'xl' for 'crystalline' so as to remove  
179 reference to a genetic mechanism (i.e., detrital) for an operationally-defined phase based  
180 on a chemical extraction procedure. We hypothesize about the origin of this phase in  
181 greater detail in the discussion.

182 To verify the efficiency of the sequential extraction method, total P ( $P_T$ ) values  
183 were determined independently (SGS Mineral Services Group) by inductively coupled  
184 plasma atomic emissions spectrometry (ICP-AES) after a standard four acid digestion  
185 (HF-HClO<sub>4</sub>-HCl-HNO<sub>3</sub>). These analyses also provide the additional major and trace  
186 metal concentrations reported below. To account for variable dilution by siliciclastic  
187 influx, we report element concentrations normalized to aluminum (Al) in wt.%/wt.% and  
188 ppm/wt.% units for major and trace elements, respectively.

189 To determine the speciation of iron within our samples, we applied a modified  
190 version of the sequential extraction method of Poulton and Canfield (2005). Here, 80-100  
191 mg of rock powder was sequentially extracted with 10 mL each of (1) 1 M sodium-  
192 acetate, adjusted to pH 4.5 with acetic acid to extract Fe associated with carbonate phases  
193 such as siderite and ankerite ( $Fe_{carb}$ ); (2) 0.28 M sodium dithionite, adjusted to pH 4.8  
194 with 0.2 M acetic acid/0.25 M tri-sodium citrate, for iron oxides such as hematite and  
195 goethite ( $Fe_{ox}$ ); and (3) 0.2 M ammonium oxalate/0.17 M oxalic acid for magnetite

196 ( $\text{Fe}_{\text{mag}}$ ). The boiling chromium reduction distillation of Canfield et al. (1986) was used to  
197 quantify sulfur (S) within pyrite from the insoluble residues derived from carbonate  
198 dissolution. We used a pyrite stoichiometry ( $\text{FeS}_2$ ) to relate the extracted S back to iron  
199 ( $\text{Fe}_{\text{py}}$ ). Total Fe ( $\text{Fe}_{\text{T}}$ ), which comprises the sum of the diagenetically highly reactive  
200 phases ( $\text{Fe}_{\text{HR}} = \text{Fe}_{\text{carb}} + \text{Fe}_{\text{ox}} + \text{Fe}_{\text{mag}} + \text{Fe}_{\text{py}}$ ), as well as unreactive Fe ( $\text{Fe}_{\text{U}}$ ; predominately  
201 silicate-bound Fe), was determined via a boiling HF-HNO<sub>3</sub>-HClO<sub>4</sub> extraction on an  
202 additional aliquot of sample powder. All iron concentrations were measured by atomic  
203 absorption spectrometry (AAS). Eight replicates of one sample, 572.64 mcd, yield a RSD  
204 of 2%, 13%, and 71% for  $\text{Fe}_{\text{carb}}$ ,  $\text{Fe}_{\text{ox}}$ , and  $\text{Fe}_{\text{mag}}$ , respectively. The high RSD of the latter  
205 two phases result from measured quantities close to the instrument detection limit; that is,  
206 the average wt.%  $\pm 1\sigma$  for the eight Fe-speciation replicates is  $0.110 \pm 0.002$ ,  $0.016 \pm 0.002$ ,  
207 and  $0.001 \pm 0.001$  for  $\text{Fe}_{\text{carb}}$ ,  $\text{Fe}_{\text{ox}}$ , and  $\text{Fe}_{\text{mag}}$ , respectively. At higher Fe concentrations for  
208 each fraction, the RSD is <5% for each stage, and this is also the case for  $\text{Fe}_{\text{py}}$  and  $\text{Fe}_{\text{T}}$   
209 (Poulton and Canfield, 2005).

210

## 211 **RESULTS**

### 212 **Lithofacies descriptions and paleoenvironmental interpretations for the Thornton**

#### 213 **Limestone and Arthur Creek Formation from drill core NTGS 99/1**

214 Markings on drill core NTGS 99/1 assign 598.4–580.1 mcd, 580.1–558.7 mcd, and  
215 558.7–554.7 mcd to the informal lower, middle, and upper members, respectively, of the  
216 Thornton Limestone (previously Hay River Formation), and 554.7–103.2 mcd to the  
217 Arthur Creek Formation (previously Marqua Formation; Ambrose et al., 2001; Dunster et  
218 al., 2007). In this study, we characterized the sedimentology and geochemistry of the

219 entire Thornton Limestone and the lowermost ~200 m of the lower Arthur Creek  
220 Formation.

221

### 222 *Thornton Limestone*

223 The Shadow Group is absent from NTGS 99/1. Here, the Thornton Limestone directly  
224 overlies Paleoproterozoic granite basement. The basal meters of the lower Thornton  
225 member include lithic fragments and sand grains within dolomudstone, with minor cubic  
226 pyrite crystals (Fig. 2a). More generally, the lower Thornton consists of dolomudstone  
227 and peloidal dolowackestone, with pervasive structural dissolution textures creating a  
228 stylolaminated to stylobedded fabric (Fig. 2b). Southgate and Shergold (1991) designated  
229 the basal, arkosic, terrigenous unit as a low-stand system tract, and the overlying stylolitic  
230 carbonate as a condensed transgressive / high-stand system tract.

231 Below 575.92 mcd (the lower Thornton Limestone) and from 580.1 - 575.92  
232 mcd (the middle Thornton Limestone), the bulk lithology is dolostone. Stratigraphically  
233 above this horizon, up to the middle–upper Thornton Limestone contact at 558.7 mcd,  
234 the bulk lithology is limestone. Nevertheless, petrographic observation of the bulk  
235 limestone lithofacies above 575.92 mcd reveals rare euhedral dolomite rhombs within an  
236 otherwise calcimudstone or calciwackestone matrix.

237 The middle Thornton contains four interbedded and interlaminated lithofacies  
238 that occur within generally coarsening-upward meter- to sub-meter-scale packages (Fig.  
239 2c). These lithofacies include: (1) black to medium gray carbonate mudstone; (2) dark to  
240 medium gray peloidal, bioclastic, and, occasionally, intraclastic wackestone; (3) medium  
241 to light gray peloidal and bioclastic packstone; and (4) medium to light gray bioclastic

242 grainstone. Carbonate mudstone or wackestone lithofacies define the base of each  
243 package and interlamine or alternate gradationally on a centimeter to decimeter scale.  
244 These carbonate mud-dominated lithologies typically grade upward into, and contact  
245 sharply with, laminae and beds of packstone. When present, thin beds of bioclastic  
246 grainstone overlie packstone beds. These grainstone beds display basal erosional contacts  
247 with millimeter to half-centimeter-scale topography, and an upper contact that is either  
248 sharp or erosional and overlain by beds of black to medium-gray carbonate mudstone. In  
249 other cases, the upper contact is diffuse and conformable with beds of medium-gray  
250 packstone or wackestone (Fig. 2d). There is a broad up-core trend: packages initiate with  
251 progressively coarser lithologies and terminate with progressively thicker grainstone  
252 beds. The nature of deposition of the Thornton Limestone within NTGS 99/1 is  
253 consistent with the phosphatic lithofacies model from the northeast Georgina Basin  
254 (Cycle mP of Southgate, 1988). Southgate and Shergold (1991) assign these shallowing-  
255 upward cycles to the transgressive system tract.

256         We interpret the lithologic association of the middle Thornton to reflect  
257 deposition within a subtidal to intertidal depositional environment. Mudstone,  
258 wackestone, and packstone beds accumulated from suspension sedimentation in calm  
259 settings that lacked significant tidal, wave, or storm activity. The coarser grain size and  
260 subtle current-generated stratification observed in grainstone beds reflect a higher energy  
261 depositional environment. Grainstone beds reveal no internal grading, but do show  
262 evidence for amalgamation and winnowing of carbonate mud by currents or waves.  
263 Deposition under the influence of waves is also manifest in rosettes of brachiopod and  
264 trilobite shell fragments along basal scour surfaces of bioclastic grainstone beds (Fig. 2d).

265 Dunster et al. (2007) interpreted the black, carbonaceous carbonates of the Thornton  
266 Formation to represent deposition under dysoxic to anoxic conditions.

267 In NTGS 99/1, the upper Thornton encompasses a 4 meter-thick vuggy,  
268 fossiliferous dolopackstone with laminae, beds, and pockets of bioclastic dolograins  
269 (Fig. 2e). When present, dolospar crystals form a mosaic around bioclasts (primarily of  
270 lingulate brachiopods). In addition to representing a prominent matrix constituent,  
271 bioclasts occur as cumulate along dissolution seams.

272 ***Petrography of apatite distribution.*** Apatite displays three predominant modes  
273 within the middle and upper Thornton Limestone. First, within bioclast-rich carbonate  
274 lithologies, apatite occurs primarily as the internal molds (steinkerns) of conical small  
275 shelly fossils or, more commonly in the upper Thornton Limestone, as lingulate  
276 brachiopod skeletal debris (Fig. 3a). Apatite also occludes gaps between, and templates  
277 the exterior of, silica-replaced skeletons (Fig. 3a). Second, in rare instances, apatite  
278 occurs as cement within bioclastic grainstone lithologies (Fig. 3b), Third, within mud-  
279 supported, suspension-deposited carbonate, apatite occurs as sub-angular to sub-rounded  
280 coarse-silt to medium-sand-size grains, and as silt- to fine-sand-size, tabular or undulose  
281 grains within well-sorted, thin beds (Fig. 3c). Due to the textural maturity and fine grain-  
282 size of these lithologies, we cannot say conclusively whether these grains were eroded,  
283 transported and winnowed from a site of apatite authigenesis (i.e., allochthonous apatite  
284 grains) or whether they were sourced with a detrital siliciclastic influx. We favor the  
285 interpretation that these grains represent re-worked authigenic grains (i.e., intraclasts of  
286 authigenic cement and steinkern bioclasts) because we observe no comparable-size

287 detrital siliciclastic grains. Below, we discuss the origin of these grains in light of  
288 geochemical data.

289

### 290 *Arthur Creek Formation*

291 Within NTGS 99/1, the basal 10 m of the lower Arthur Creek encompasses a petroleum-  
292 generating, massive black shale (Fig. 2e), or ‘hot shale’ (e.g., Dunster et al., 2007),  
293 succeeded by planar, undulose, and corrugated interlaminae of black to dark gray organic  
294 matter- and clay-rich shale and siltstone with medium to light gray calcimudstone and  
295 dolomudstone. This shale also contains rare interbeds of very fine-grained bioclastic  
296 packstone and grainstone (Fig. 2f). Clay- and iron-oxide-rich laminae include sub-  
297 rounded to angular, very well sorted, monocrystalline quartz and authigenic pyrite  
298 crystals, the latter of which often occlude pore space. Horizontal alignment of clay  
299 minerals indicates that compaction enhanced the physical expression of lamination.  
300 Commonly below ~490 mcd, and only rarely above, decimeter-scale light gray limestone  
301 nodules displace surrounding laminations and retain faint remnants of lamination,  
302 indicating nodular development during compaction, but before lithification (Fig. 2g). We  
303 interpret individual laminae to reflect the gravitational settling of fine particles suspended  
304 by dilute turbidity currents that wafted sediment towards the basin interior, consistent  
305 with an outer-ramp depositional environment (Dunster et al., 2007). The fetid,  
306 carbonaceous black shale and black, carbonaceous, laminated dolostone suggest  
307 deposition under dysoxic to anoxic conditions (Dunster et al., 2007).

308         In the upper meters of the measured lower Arthur Creek, a second lithofacies  
309 interbeds with the laminated facies (Fig. 2h). This facies includes interbeds of light gray

310 calcimudstone and siliciclastic siltstone. Rare truncation of undulatory laminae indicates  
311 intermittent deposition under the influence of currents. This facies is a harbinger of the  
312 more proximal, oxygenated ramp environment of the overlying upper Arthur Creek  
313 Formation (Dunster et al., 2007), which was not measured in this study. Southgate and  
314 Shergold (1991) assign the lower Arthur Creek to a transgressive system tract.

315

### 316 **Geochemistry of the Thornton Limestone and Arthur Creek Formation**

317 A generalized stratigraphic column of the Thornton and lower Arthur Creek is shown in  
318 Figure 4a alongside chemostratigraphic variation in  $\delta^{13}\text{C}_{\text{carb}}$  (Fig. 4b),  $\delta^{18}\text{O}_{\text{carb}}$  (Fig. 4c)  
319 and  $\delta^{13}\text{C}_{\text{org}}$  (Fig. 4d). Cross-plots of  $\delta^{13}\text{C}_{\text{carb}}$  and  $\delta^{18}\text{O}_{\text{carb}}$  display no statistically  
320 significant co-variation (Fig. 4e), thereby suggesting that  $\delta^{13}\text{C}_{\text{carb}}$  values, at least,  
321 represent the primary seawater isotopic composition. The  $\delta^{13}\text{C}_{\text{carb}}$  curve generated for  
322 NTGS 99/1 displays two positive peaks, the first in the middle Thornton (563.92 mcd)  
323 and the second in the Arthur Creek (506.51 mcd). Consistent with trilobite  
324 biostratigraphy (Laurie, 2004a,b), we correlate the middle Thornton excursion to the  
325 Ordian–early Templetonian isotopic event and the Arthur Creek excursion to the Late  
326 Templetonian–Floran event (Fig. 4b; Lindsay et al., 2005). This assignment corroborates  
327 regional isotopic variation in the southern Georgina, Amadeus, and Daly Basins (Lindsay  
328 et al., 2005) and, further afield, to the Argentine Precordillera (Gomez et al., 2007), the  
329 Great Basin, U.S.A. (Saltzman, 2005), South China (Zhu et al., 2004; Guo et al., 2010),  
330 and northwest China (Wang et al., 2011).

331 Small magnitude discontinuities in  $\delta^{13}\text{C}_{\text{carb}}$  chemostratigraphy occur across the  
332 informal member boundaries of the Thornton Limestone (Fig. 4b). These

333 discontinuities likely represent erosive events or hiatuses in deposition. In support of the  
334 former interpretation, an increase in Zr/Al occurs across the middle/upper Thornton  
335 contact (Supplementary Figure 1). Elevated Zr/Al ratios define erosional surfaces where  
336 high-energy currents winnow fine-grained, low-density siliciclastics (characterized by  
337 Al) and concentrate high-density minerals (characterized by Zr; Vine and Tourtelot,  
338 1970). Unlike carbon isotopes, secondary fluid migration does not affect the Zr/Al ratio.  
339 Thus, this proxy confirms sediment winnowing during deposition of the upper  
340 Thornton. Regionally, the Thornton Limestone—Arthur Creek Formation contact  
341 represents a sequence boundary, with karstification developed along this surface in the  
342 western margin of the basin (Dunster et al., 2007). While the formation boundary within  
343 NTGS 99/1 represents a sharp lithologic break,  $\delta^{13}\text{C}_{\text{carb}}$  values display general continuity  
344 across this boundary (Fig. 4b), suggesting either relative temporal continuity or fortuitous  
345 resumption of deposition with similar carbon isotopic composition. Isopach maps of the  
346 Arthur Creek show that the formation thickens to the east-southeast, where the NTGS  
347 99/1 drill core intercepted the maximum depocenter of the preserved basin margin  
348 (Dunster et al., 2007). Thus, under the former scenario, the Thornton Limestone—  
349 Arthur Creek Formation boundary within NTGS 99/1 could represent a correlative  
350 conformity of the regional sequence boundary, with limited time missing across this  
351 lithologic contact.

352         Within NTGS 99/1,  $\delta^{13}\text{C}_{\text{org}}$  displays co-variation with  $\delta^{13}\text{C}_{\text{carb}}$  within the lower  
353 Thornton Limestone and no co-variation with  $\delta^{13}\text{C}_{\text{carb}}$  within either the middle/upper  
354 Thornton or the Arthur Creek formations (Fig. 4d,f; lower Thornton:  $R^2 = 0.75$ ;  
355 middle/upper Thornton:  $R^2 = 0.04$ ; Arthur Creek:  $R^2 = 0.2$ ). TOC varies from 0.1-2.9



356 wt.% in the Thornton, displaying a generally increasing trend in the lower Thornton  
357 and high variance in the middle Thornton. TOC ranges from 0.1 to 2.5 wt.% in the  
358 lower Arthur Creek, with higher values at the base of the formation, decreasing towards a  
359 mean of 0.1 wt.% TOC in the upper 100 m of the measured core interval (Fig. 4d).  
360 Despite the lack of covariance between  $\delta^{13}\text{C}_{\text{carb}}$  and  $\delta^{13}\text{C}_{\text{org}}$  in strata of the middle/upper  
361 Thornton and the Arthur Creek Formation, one trend emerges: high (> 1.0 wt.%),  
362 medium (0.2 < wt.% < 1.0), and low (< 0.2 wt. %) TOC correlate with light,  
363 intermediate, and heavy  $\delta^{13}\text{C}_{\text{org}}$  values (Fig. 4d). That is, the lightest  $\delta^{13}\text{C}_{\text{org}}$  values occur  
364 in the most organic- and phosphorus-rich lithofacies, the middle Thornton Limestone  
365 (*cf.*, Bartley et al., 1998, and Guo et al., 2013). The latter two TOC bins generally  
366 correspond to samples from the Arthur Creek below and above ~430 mcd, respectively,  
367 which is the transition between the laminated facies and the interbedded carbonate  
368 mudstone–siliciclastic shale and siltstone facies.

369 Total phosphorus ( $P_T$ ) within the Thornton Limestone ranges up to 3.9 wt.%  
370 (Fig. 5a).  $P_T$  increases systematically within the lower Thornton and the lowermost  
371 middle Thornton, followed by an additional increase around 575 mcd. We note that the  
372 transition from dolostone (stratigraphically below 575.92 mcd) to limestone  
373 (stratigraphically above 575.92 mcd) within drill core NTGS 99/1 occurs just below this  
374 jump in P content (Figs 5a,b). The overlying meters of the middle and upper Thornton  
375 display high variance in  $P_T$ . In contrast, the maximum value of  $P_T$  within the Arthur  
376 Creek is 0.4 wt.%, but is typically much lower with a median of 0.03 wt.% and 1<sup>st</sup> and 3<sup>rd</sup>  
377 quartile values of 0.02 and 0.04 wt.%, respectively (Fig. 5a).

378 We tested the fidelity of the P sequential extraction method by comparing the sum  
379 of the operationally-defined pools ( $P_T = P_{xl} + P_{auth+carb} + P_{org} + P_{Fe}$ ) to the total  
380 phosphorus content determined by ICP-AES analysis. The consistency between these two  
381 measurement techniques (slope of linear regression = 1.1,  $R^2 = 0.88$ ; Fig. 5e) increases  
382 confidence in the values of the constituent sequential extraction phases. In both the  
383 Thornton Limestone and the Arthur Creek Formation, the operationally-defined  $P_{xl}$  and  
384  $P_{auth+carb}$  phases dominate  $P_T$ , while  $P_{org}$  and  $P_{Fe}$  contribute a negligible fraction (Fig. 5b).  
385 The median (1<sup>st</sup>, 3<sup>rd</sup> quartile) percent contribution to  $P_T$  are:  $P_{xl} = 91.5\%$  (77.5, 94.4),  
386  $P_{auth+carb} = 7.5\%$  (3.7, 19.5), and  $P_{org} = 0.4\%$  (0.2, 1.5).  $P_{Fe}$  was measured only on a subset  
387 of samples, but this phase contributes minimally to  $P_T$  (a median of 0.1% with 1<sup>st</sup> and 3<sup>rd</sup>  
388 quartiles of 0.0 and 0.4%, respectively).

389 Total iron ( $Fe_T$ ) varies from 0.06-1.49 wt.% in the Thornton Limestone and  
390 from 0.32-2.71 wt.% in the Arthur Creek Formation (Fig. 5c). In general,  $Fe_T$  is lowest  
391 where  $P_T$  is highest. Based on the slope of linear regression, 88% of  $Fe_T$  resides in  $Fe_{HR}$   
392 phases within the Thornton ( $R^2 = 0.92$ ; Fig. 6a). In contrast, within the Arthur Creek,  
393 ~48% of  $Fe_T$  resides in  $Fe_{HR}$  ( $R^2 = 0.57$ ; Fig. 6a), consistent with the higher siliciclastic  
394 fraction for these lithologies. The lower coefficient of determination for the Arthur Creek  
395 Formation reflects a decrease in  $Fe_{HR}/Fe_T$  from 0.66 at the base of the formation to ~0.3  
396 near the top of the measured core interval. Reduced iron phases,  $Fe_{py}$  and  $Fe_{carb}$ , dominate  
397  $Fe_{HR}$  in both formations, while oxidized and partially oxidized iron phases,  $Fe_{ox}$  and  
398  $Fe_{mag}$ , contribute a minimal fraction (Fig. 5c). Based on the slope of the linear regression,  
399 82% of  $Fe_{HR}$  resides as  $Fe_{carb}$  within the lower Thornton ( $R^2 = 0.62$ ; Fig. 6c) while  $Fe_{py}$   
400 accounts for only a minor contribution that has no statistically significant correlation with

401  $Fe_{HR}$  (Fig. 6b). As such, the gradual decrease in  $Fe_{HR}$  within the lower Thorntonite reflects  
402 a systematic decrease in  $Fe_{carb}$  from very high values of 1.3 wt.%, to ~0.3 wt.%. In the  
403 middle and upper Thorntonite, 64% of  $Fe_{HR}$  resides as  $Fe_{py}$  ( $R^2 = 0.95$ ; Fig. 6b) and 31%  
404 resides as  $Fe_{carb}$  ( $R^2 = 0.82$ ; Fig. 6c). For the lower Arthur Creek, ~73% and 26% of  $Fe_{HR}$   
405 reside in  $Fe_{py}$  ( $R^2 = 0.94$ ; Fig. 6b) and  $Fe_{carb}$  ( $R^2 = 0.72$ ; Fig. 6c), respectively.

406         When we parse the Fe-speciation data of the middle Thorntonite Limestone  
407 samples by lithology, we see a similar partitioning of Fe phases as when we group all  
408 samples within members (as presented above). Within the dolostone of the middle  
409 Thorntonite (580.1 – 575.92 mcd), 98% of  $Fe_T$  resides in  $Fe_{HR}$  ( $R^2 = 0.99$ ); in contrast,  
410 within the limestone of the middle Thorntonite (575.92 mcd – 558.7 mcd), 89% of  $Fe_T$   
411 resides in  $Fe_{HR}$  ( $R^2 = 0.95$ ). Likewise, within middle Thorntonite dolostone, 67% ( $R^2 =$   
412 0.94) and 27% ( $R^2 = 0.69$ ) of  $Fe_{HR}$  resides in  $Fe_{py}$  and  $Fe_{carb}$ , respectively; within the  
413 middle Thorntonite limestone, 68% ( $R^2 = 0.96$ ) and 30% ( $R^2 = 0.86$ ) of  $Fe_{HR}$  resides in  
414  $Fe_{py}$  and  $Fe_{carb}$ , respectively.

415         Within NTGS 99/1, the median (1<sup>st</sup>, 3<sup>rd</sup> quartile) percent acid insoluble fraction  
416 (i.e., silicates) within the Thorntonite is 8.3% (5.3, 17.0) as compared to 44.0% (32.8,  
417 54.3) for the Arthur Creek (Supplementary Figure 1). TOC/Al ratios are higher and more  
418 variable in the Thorntonite than for the Arthur Creek (Supplementary Figure 1). Fe/Al  
419 ratios and Mn/Al ratios decline throughout the lower Thorntonite (save for a couple of  
420 high values in the upper Thorntonite; Supplementary Figure 1). The detrital-associated  
421 trace element ratio Zr/Al is low and variable within the Thorntonite compared to the  
422 Arthur Creek Formation and displays an abrupt increase across the middle/upper  
423 Thorntonite boundary. (See Supplementary Information for a discussion of aluminum-

424 normalized concentrations of redox-sensitive and bioessential trace metals;  
425 Supplementary Figure 2.)

426

## 427 **DISCUSSION**

428 How do these geochemical data inform our understanding of the source of phosphorus to  
429 phosphatic *Thorntonia* carbonates and, more broadly, the loss of phosphatic lithologies  
430 and consequent closure of the phosphatization taphonomic mode during Cambrian Series  
431 2? To address these questions, we combine petrographic observations with P-speciation  
432 data to quantify authigenic apatite within the *Thorntonia* Limestone. In turn, we explore  
433 the possibility that P bound within bioclasts, organic matter, or iron minerals sourced the  
434 observed P within these lithologies. Finally, we present a mathematical framework for  
435 which to deconvolve the relative contribution of the two most likely sources—P bound  
436 with organic matter or iron minerals—to authigenic apatite nucleation.

437

### 438 **Source(s) of phosphorus to the *Thorntonia* Limestone and Arthur Creek Formation**

439 How much of the apatite within the *Thorntonia* Limestone and Arthur Creek Formation  
440 must we account for with P delivery shuttles? Phosphorus speciation provides a  
441 (semi)quantitative measure of the partitioning of phosphorus within a sedimentary  
442 succession. The majority of P extracted from NTGS 99/1 is operationally classified as  
443 fluorapatite of detrital igneous and/or metamorphic origin ( $P_{xl}$ ; Ruttenger, 1992) and  
444 constitutes a median (1<sup>st</sup>, 3<sup>rd</sup> quartile) of 91.5% (77.5, 94.4) of  $P_T$ . However, we have  
445 three reasons to question this genetic interpretation. First, as described above,  
446 petrographic observations reveal that apatite within the *Thorntonia* Limestone occurs

447 predominantly as the internal molds of small shelly fossils (Fig. 3a) or, occasionally, as  
448 cement within bioclastic grainstone (Fig 3b), both indications of an authigenic origin.  
449 Given the thermal history of the Georgina Basin, which reached temperatures necessary  
450 to develop Type II kerogen (Dunster et al., 2007), burial diagenesis should have increased  
451 the crystallinity of authigenic phosphate minerals (Shemesh, 1990). It is thus not  
452 surprising that authigenic apatite formed within marine sediment during the Cambrian is  
453 now operationally classified as crystalline igneous and metamorphic apatite (*sensu* Föllmi  
454 et al., 2005). Second, within mud-supported, suspension-deposited carbonate, apatite  
455 occurs as coarse-silt- to medium-sand-size grains. Given that we observe no comparable  
456 size detrital siliciclastic grains, we suggest these grains are eroded, transported and  
457 winnowed authigenic grains. Third, if the  $P_{x1}$  phase comprised fluorapatite sourced to the  
458 basin along with a detrital siliciclastic influx, we would predict that it should correlate  
459 with the siliciclastic-associated heavy element Zr/Al ratio. We observe no correlation  
460 between  $P_{x1}$  and Zr/Al (Fig. 5f). Thus, consistent with petrographic observations, we  
461 conclude that the  $P_{x1}$  pool largely represents authigenic apatite and, therefore, we must  
462 account for this phase with a delivery shuttle of P to the sediment column.

463

#### 464 **Bioclastic apatite as a source of phosphorus for authigenic apatite precipitation?**

465 Lingulid brachiopods comprise a fraction of the bioclasts identified in samples analyzed  
466 petrographically for carbonate sedimentology and apatite distribution. The presence of  
467 these phosphatic bioclasts raises two issues. First, samples that contain apatite bioclasts  
468 will have a wt.%  $P_T$  that overestimates the quantity of authigenic apatite. Determining the  
469 actual wt.% of P within authigenic apatite for these samples would require subtracting the

470 wt.% of bioclastic P from the bulk wt.%  $P_T$  determined by phosphorus speciation  
471 geochemistry. One method for determining the wt.% of P within primary phosphatic  
472 bioclasts would be to use quantitative point-count data to determine the volume of  
473 bioclasts, then to multiply this volume by the density of dahllite to determine the mass  
474 (wt.%) of P. Given that the percent of primary phosphatic bioclasts visually  
475 (qualitatively) rarely exceeds the percent of phosphatic steinkerns and sand-sized  
476 authigenic grains (see discussion above), we move forward without quantitative estimates  
477 of the wt.% of bioclastic P under the caveat that, for lingulid brachiopod-bearing  
478 bioclastic lithologies,  $P_T$  overestimates authigenic apatite within a sample.

479         Second, the observation of bioclasts of primary phosphatic shells raises the  
480 possibility that *in situ* dissolution of these bioclasts may have contributed to high pore-  
481 water phosphate concentration and facilitated subsequent authigenic precipitation.  
482 However, petrographic observations show that inarticulate brachiopod and other  
483 phosphatic skeletons are not unusually abundant in phosphate-rich Thorntonina horizons,  
484 and conversely that authigenic phosphate is not unusually abundant in those samples with  
485 the highest abundances of phosphatic skeletons. Nor do these remains show marked  
486 evidence of dissolution. Thus, the sedimentation of phosphatic skeletal material does not  
487 seem capable of sourcing the phosphate now found in Thorntonina rocks. Further, *in situ*  
488 dissolution of phosphatic bioclasts would necessitate pore fluids that promoted the early  
489 dissolution of apatite shells without concurrent dissolution of the calcium carbonate  
490 shells and sediment molded and/or replaced by the precipitation of authigenic calcium  
491 phosphate minerals. For these reasons, we do not invoke phosphatic skeleton-derived P as  
492 a significant source for authigenic apatite precipitation. Nevertheless, if phosphatic

493 skeleton dissolution were to have sourced P for authigenic apatite, then the required  
494 quantity of organic and iron-bound P (discussed below) would lessen proportionately.

495

496 **Organic-bound phosphorus as a source of phosphorus for authigenic apatite**  
497 **precipitation?**

498 Particulate organic carbon represents the main delivery shuttle of phosphorus to the  
499 sediment column in the modern ocean (e.g., Delaney, 1998; Benitez-Nelson, 2000), and  
500 so we ask whether organic carbon could have sourced the observed amount of P within  
501 beds of the Thornton Limestone and the Arthur Creek Formation. Perhaps the simplest  
502 model for organic-bound P delivery is to assume that organic matter arrived at the sea  
503 floor with a Redfield  $C_{org}:P_{org}$  molar ratio of ~106:1 (Redfield, 1958). However,  $C_{org}:P_{org}$   
504 of organic matter within marine sediment and, therefore, sedimentary rocks, is commonly  
505 much higher than the Redfield ratio as a result of the preferential remineralization of P-  
506 rich organic compounds within the water-column (Clark et al., 1998) or within the  
507 sediment column (Ingall et al., 1993, Ingall and Jahnke, 1997; Van Cappellen and Ingall,  
508 1996; Jilbert et al., 2011).  $C_{org}:P_{org}$  molar ratios within the Thornton Limestone range  
509 from 79:1 up to 17,000:1 [median (1<sup>st</sup>, 3<sup>rd</sup> quartile) = 1,389:1 (521:1, 3619:1)]. Likewise,  
510  $C_{org}:P_{org}$  molar ratios within the Arthur Creek Formation range from 43:1 up to 11,770:1  
511 [median (1<sup>st</sup>, 3<sup>rd</sup> quartile) = 903:1 (360:1, 3,372:1)]. Thus,  $C_{org}:P_{org}$  molar ratios within  
512 these lithologies deviate substantially from the Redfield ratio and, at face value, suggest  
513 extensive preferential  $P_{org}$  loss during organic matter respiration.

514         When organic respiration occurs within the sediment column, liberated  $P_{org}$  may  
515 ‘sink-switch’ and precipitate as authigenic phosphate minerals (Ruttenberg and Berner,

516 1993), as is likely the case for the development of phosphatic strata within the Thornton  
517 Limestone. With respect to phosphorus speciation terminology, ‘sink-switching’ would  
518 transfer P from the  $P_{\text{org}}$  phase to either the authigenic  $P_{\text{xl}}$  or the  $P_{\text{auth+carb}}$  phase. In that  
519 regard,  $C_{\text{org}}:P_{\text{T}}$  should provide a better estimate of the retention of organic-bound P to the  
520 sedimentary environments of the Thornton Limestone and Arthur Creek Formation  
521 (Ingall et al., 1993; Ruttenger and Berner, 1993; Anderson et al., 2001; Algeo and Ingall,  
522 2007).  $C_{\text{org}}:P_{\text{T}}$  ranges from 0.1–16:1 within the Thornton Limestone with a median (1<sup>st</sup>,  
523 3<sup>rd</sup> quartile) value of 2.5:1 (1.2:1, 4.8:1). For the non-phosphatic Arthur Creek Formation,  
524  $C_{\text{org}}:P_{\text{T}}$  ranges from 5–157:1 with a median (1<sup>st</sup>, 3<sup>rd</sup> quartile) value of 17.4:1 (7.6:1,  
525 44.5:1). Thus, with the exception of four samples,  $C_{\text{org}}:P_{\text{T}}$  molar ratios for both the  
526 Thornton Limestone and the Arthur Creek Formation fall well below the canonical  
527 Redfield ratio (Fig. 5d). From this perspective, both the Thornton Limestone and the  
528 Arthur Creek Formation retain more P than would be expected based on organic matter  
529 delivery with a molar  $C_{\text{org}}:P_{\text{org}}$  ratio equal to or greater than the Redfield ratio.

530         Preferential  $C_{\text{org}}$  remineralization or hydrocarbon migration relative to P retention  
531 may have resulted in a molar C: $P_{\text{T}}$  lower than the Redfield ratio. The required > 90% loss  
532 of  $C_{\text{org}}$  (see below) appears to be common in relatively organic-lean sediment deposited  
533 on oxic Cenozoic seafloors (Anderson et al., 2001); however, given the organic carbon  
534 content of Thornton samples, and accepting sedimentological and geochemical  
535 arguments for anoxic deposition of the Thornton Limestone (see below), such loss  
536 would have required massive remineralization under anoxic pore water conditions.  
537  $\delta^{13}\text{C}_{\text{carb}}$  values do not show the distinctly light values that might be expected in this  
538 circumstance (Schrag et al., 2013). Assuming that all phosphorus was delivered via



539 organic matter with a Redfield ratio and was subsequently retained within the sediment  
540 column, the discrepancy between the Redfield ratio and the measured C:P<sub>T</sub> provides a  
541 minimum estimate of C<sub>org</sub> loss (estimated quantitatively in a later section).

542       Organic carbon loss may also occur during low-grade metamorphism (Raiswell  
543 and Berner, 1987). Since the lithology of the Thornton Limestone precludes a confident  
544 application of the suggested metrics to account for this loss (Raiswell and Berner, 1987),  
545 we cannot evaluate how much this process may have contributed to the discrepancy  
546 between measured C<sub>org</sub>:P<sub>T</sub> values and the Redfield ratio. However, we can explore  
547 whether an additional phosphorus delivery shuttle augmented organic-bound P delivery  
548 to the sea floor during deposition of the Thornton Limestone and Arthur Creek  
549 Formation. We discuss this possibility in a later section.

550       Notably, phosphatic strata of the middle Thornton Limestone have the highest  
551 measured wt. % TOC and the lightest  $\delta^{13}\text{C}_{\text{org}}$  values preserved within this sedimentary  
552 succession (Fig. 4c). A similar relationship has been documented in Proterozoic basins and  
553 attributed to differential recycling of organic matter in benthic mats (e.g., Bartley et al.,  
554 1998; Guo et al., 2013). Within the Thornton Limestone, this relationship may result  
555 from a difference in the primary isotopic composition of organic matter sourcing  
556 phosphatic strata, from variable *in situ* remineralization of the sedimentary organic  
557 carbon reservoir, or from some combination of these two processes. We do not have an  
558 independent line of evidence (e.g., compound specific biomarkers) to distinguish between  
559 these possibilities. Instead, we note that acceptance of either of these hypotheses to  
560 explain the observed correlation between P content and  $\delta^{13}\text{C}_{\text{org}}$  values makes a prediction  
561 for the mechanism of P delivery. For the case of an isotopically distinct organic carbon

562 source to the middle Thornton Limestone, the C:P ratio of this source must have been  
563 much lower than the canonical Redfield ratio of 106C:1P. For the case of limited C<sub>org</sub>  
564 remineralization within phosphatic strata, an alternative P delivery shuttle to the sediment  
565 column must have augmented organic-bound P delivery.

566

567 **Iron-bound phosphorus as a source of phosphorus for authigenic apatite**  
568 **precipitation?**

569 If our estimates of organic-bound P delivery fail to account for the phosphate necessary  
570 for the observed Thornton apatite content, what alternative source could supply this P?  
571 A growing body of literature calls upon P adsorbed to the surface or co-precipitated with  
572 metal oxides, particularly iron (oxyhydr)oxide particles, as an important shuttle of  
573 phosphorus to the sea floor (Berner, 1973; Shaffer, 1986; Feely et al., 1991; Feely et al.,  
574 1998; Poulton and Canfield, 2006). Additionally, under anoxic conditions, Fe(II)-  
575 phosphates (e.g., vivianite, strengite) may play a more important role for marine P  
576 cycling than previously considered (e.g., März et al., 2008; Dellwig et al., 2010; Jilbert  
577 and Slomp, 2013). Thus, the release of adsorbed/co-precipitated Fe-bound P to sediment  
578 pore waters has previously been invoked as a necessary and significant source of P for  
579 sedimentary apatite nucleation (Krom and Berner, 1981; Schuffert et al., 1994, 1998;  
580 Slomp et al., 1996; Shen et al., 2000; März et al., 2008; Jilbert and Slomp, 2013).

581        Could the Fe-P shuttle have augmented organic-bound P delivery to Thornton  
582 and Arthur Creek sediments? In the modern, oxygenated ocean, iron mobility is generally  
583 limited to particulate fluxes of insoluble Fe<sup>3+</sup> phases (Martin and Meybeck, 1979;  
584 Poulton and Raiswell, 2002). Under these conditions, we might predict Fe-bound P

585 delivery to these environments to be proportional to the (predominantly siliciclastic)  
586 particulate Fe(III) flux. In contrast, under anoxic conditions the reductive dissolution of  
587 iron (oxyhydr)oxides by dissimilatory iron reduction or by dissolved sulfide during early  
588 diagenesis generates soluble  $\text{Fe}^{2+}$  that is subsequently redistributed to anoxic slope and  
589 basinal environments (Canfield et al., 1996; Severmann et al., 2008; 2010; see review in  
590 Lyons and Severmann, 2006). This so-called ‘intrabasin iron shuttle’ provides a  
591 mechanism for decoupling iron delivery to the seafloor from siliciclastic sources and,  
592 therefore, we hypothesize that it allows for the delivery of P adsorbed to detrital Fe(III)  
593 minerals, Fe(II)-phosphate minerals (e.g., März et al., 2008; Dellwig et al., 2010; Jilbert  
594 and Slomp, 2013) and P adsorbed to/co-precipitated with Fe(III)-minerals formed from  
595 the oxidation of ferrous iron in the water column (*cf.*, Mayer and Jarrell, 2000). In this  
596 regard, under either an oxic or an anoxic Cambrian water-column, Thornton and Arthur  
597 Creek sediments could have received substantial Fe-bound P; however, we note that the P  
598 contribution from the Fe-bound P shuttle would have been larger if these sediments  
599 accumulated under an anoxic water column.

600         The redox state of the southern Georgina Basin water column during deposition of  
601 these middle Cambrian strata can be assessed using data on the speciation and enrichment  
602 of sedimentary iron minerals. This geochemical method is most commonly applied to  
603 fine-grain siliciclastic lithologies, where the ratios of various mineralogical phases are  
604 interpreted to reflect specific and calibrated environmental redox conditions (Canfield et  
605 al., 1992; Raiswell and Canfield, 1998; Raiswell et al., 2001; Poulton and Raiswell,  
606 2002). On the basis of empirical evidence,  $\text{Fe}_{\text{HR}}/\text{Fe}_{\text{T}}$  above 0.38 within fine-grain  
607 siliciclastic lithologies indicates sediment accumulation under an anoxic water-column

608 (Raiswell and Canfield, 1998; Raiswell et al., 2001; Poulton and Raiswell, 2002), while  
609  $Fe_{HR}/Fe_T$  below a value of  $\sim 0.22$  is suggestive of oxic conditions (Poulton and Raiswell,  
610 2002; Poulton and Canfield, 2011); additionally, in the case of anoxia,  $Fe_{py}/Fe_{HR}$   
611 differentiates ferruginous ( $<0.7-0.8$ ) from euxinic ( $>0.8$ ) conditions (Anderson and  
612 Raiswell, 2004; Poulton et al., 2004; März et al., 2008; Poulton and Canfield, 2011).

613         The Arthur Creek Formation includes a siliciclastic facies (the ‘hot shale’) that is  
614 ideal for iron-based redox proxies (Poulton and Canfield, 2005).  $Fe_T$  within the Arthur  
615 Creek ‘hot shale’ ranges up to  $\sim 2.7$  wt.% (Fig. 6a) and almost all measured highly  
616 reactive iron resides in reduced iron minerals (Fig. 6b,c).  $Fe_{HR}/Fe_T$  and  $Fe_{PY}/Fe_{HR}$   
617 indicate an anoxic, ferruginous redox environment during deposition of the ‘hot shale’  
618 (Fig. 6a,b). In contrast, strata of the interlaminated siliciclastic shale/siltstone and  
619 carbonate calcimudstone facies of the Arthur Creek Formation (directly overlying the  
620 ‘hot shale’) contain a lower siliciclastic component, and this requires special attention in  
621 interpreting a paleo-redox environment. We note that each iron-speciation sample  
622 integrates 3 cm of stratigraphy; therefore, for this lithofacies, our sample preparation  
623 method homogenized multiple laminae of pure siliciclastic shale/siltstone and pure  
624 carbonate mudstone. Yet, despite the diluting carbonate component,  $Fe_{HR}$  is partitioned  
625 within this lithofacies in the same proportionality as the ‘hot shale’ (Fig. 6b,c). In this  
626 regard, iron speciation data for this lithofacies of the Arthur Creek Formation are  
627 consistent with the anoxic, ferruginous redox environment inferred for the underlying  
628 ‘hot shale’.

629         Strata of the Thornton Limestone are composed almost entirely of carbonate,  
630 and for this reason we do not to interpret these iron speciation data within the canonical,

631 siliciclastic-derived redox framework. Instead, we emphasize that the black, organic-rich  
632 carbonate strata of the middle/upper Thornton Limestone (Fig. 2c), biomarker and  
633 organic geochemistry of the Thornton and Arthur Creek petroleum systems (Boreham  
634 and Ambrose, 2005), and trace element data (Supplementary Information) are  
635 qualitatively consistent with iron speciation metrics for the Arthur Creek Formation ‘hot  
636 shale’ (Fig. 6) for an anoxic depositional environment during accumulation of the  
637 phosphatic middle/upper Thornton Limestone. Thus, we conclude that the Fe-oxide  
638 bound P shuttle likely augmented organic-bound P delivery to the Thornton and Arthur  
639 Creek sediment column. Further, if one accepts the sedimentological and geochemical  
640 evidence for sediment accumulation under an anoxic, ferruginous water column, this then  
641 allows for the possibility that Fe(II)-phosphates provided a second, potentially significant  
642 source of P to Thornton sediments.

643         Nevertheless, the limited contribution of  $Fe_{ox}$  to  $Fe_{HR}$  in both the Thornton and  
644 Arthur Creek (Fig. 5c), the low  $P_{Fe}$  values (Fig. 5b), and the present decoupling of P  
645 within the Thornton from  $Fe_{HR}$  phases (Fig. 5g) all suggest that any P delivered to  
646 Thornton sediments via the Fe-P shuttle must have been subsequently decoupled from  
647 iron particles within the sediment column. One way to explain this decoupling is through  
648 the reductive dissolution of Fe oxides in anoxic pore-waters. This suggestion is consistent  
649 with petrological observations that require wholesale remobilization of P before  
650 precipitation within shell interiors (Fig. 3a,b). Thus, the present distribution of P in the  
651 Thornton Limestone, spatially decoupled from either iron or organic carbon sources,  
652 confounds easy attribution to primary source vectors. In the following section we

653 integrate C, Fe, and P geochemical data to explore the relative contribution from organic-  
654 bound and iron-bound P delivery sources.

655

656 **Assessing the relative importance of organic-bound versus iron-bound phosphorus**  
657 **to authigenic apatite precipitation**

658 To begin, we estimate whether organic matter degradation alone could provide sufficient  
659 phosphorus for the observed apatite content in the Thornton Limestone. We then  
660 quantify how much of this estimated organic carbon must have been lost through  
661 remineralization to reconcile the observed wt.% TOC within these strata. To do so, we  
662 use a Redfield stoichiometry (Redfield, 1958) to relate the measured sedimentary weight  
663 percent phosphorus to the associated flux of organic carbon necessary for this phosphorus  
664 delivery. Redfield stoichiometry varies in space and time due to, for instance, taxonomic  
665 variability in biomolecular and cellular composition and nutrient availability regulating  
666 biosynthetic allocation (e.g., Geider and LaRoche, 2002). Moreover, water-column  
667 heterotrophy increases the C:P ratio of particulate organic carbon delivered to the  
668 sediment-water interface (Clark et al., 1998). To be conservative, we assume no water-  
669 column remineralization and adopt the canonical Redfield ratio (106C:1P) in the  
670 calculations below. We also adopt the combined organic-bound and authigenic  
671 phosphorus phases determined from the phosphorus speciation extraction as an estimate  
672 of the original flux of phosphorus delivered to the sediment via organic matter. This  
673 calculation provides a conservative estimate because we neglect iron-adsorbed and  
674 carbonate-bound P as potential sources for authigenic apatite (as these can represent

675 primary sources of phosphorus to the sediment column), and we assume no diffusive loss  
676 of phosphate from pore-water contemporaneous with sedimentary apatite authigenesis.

677 Following the above arguments, our estimate for the weight percent organic  
678 carbon delivered to the sediment column ( $\hat{C}_{org}^*$ ) that can account for the measured  
679 phosphorus content is given by:

$$680 \quad \hat{C}_{org}^* = (P_{xl} + P_{org}) \times R \times \left( \frac{\alpha_c}{\alpha_p} \right) \quad (1)$$

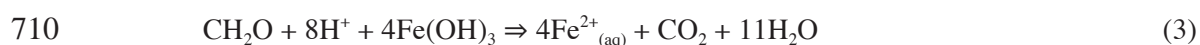
681 where R is the adopted Redfield ratio and  $\alpha_C$  and  $\alpha_P$  represent the molar weights of  
682 carbon and phosphorus, respectively (Slomp et al., 2004). We estimate the percentage of  
683 organic carbon remineralization necessary to reconcile the difference between the  
684 delivery estimate,  $\hat{C}_{org}^*$ , and the measured wt.% total organic carbon ( $C_{org}$ ) within  
685 Thornton and Arthur Creek rocks (Slomp et al., 2004) as:

$$686 \quad \% \text{ loss of } \hat{C}_{org}^* = \left( \frac{\hat{C}_{org}^* - C_{org}}{\hat{C}_{org}^*} \right) \times 100 . \quad (2)$$

687 This value represents an estimate of organic carbon remineralization in the time between  
688 delivery to the sediment-water interface and lithification. Applying these equations to  
689 samples within the phosphorus-enriched middle and upper Thornton yields a median  
690  $\hat{C}_{org}^*$  of 18.6 wt.% and a median loss of 97.8% of this estimated delivery flux (Fig. 7). For  
691 comparison, applying these equations to samples from the Arthur Creek indicates a  
692 median organic carbon loss estimate of 74.0% from a median organic carbon delivery  
693 estimate,  $\hat{C}_{org}^*$ , of only 1.1 wt.% (Fig. 7). If, instead, we consider more typical ratios of  
694  $C_{org}:P_{org}$  delivered to the sediment column, that is, C:P  $\gg$  106:1 (Ingall et al., 1993; Van  
695 Cappellen and Ingall, 1996; Clark et al., 1998; Algeo and Ingall, 2007), then the required

696  $C_{org}$  delivery ( $\hat{C}_{org}^*$ ) and the estimated %  $\hat{C}_{org}^*$  loss increase proportionally. Likewise, any  
 697 diffusive/advective loss of phosphate from the sediment column prior to lithification  
 698 (Ingall et al., 1993; Slomp et al. 2002; 2004) would increase the requisite  $\hat{C}_{org}^*$  and, thus,  
 699 the inferred %  $\hat{C}_{org}^*$  loss.

700 If organic carbon represented the sole delivery source of phosphorus to the  
 701 sediment column, what would have been the oxidant demand for the organic carbon  
 702 remineralization estimated above? Dissimilatory microbial metabolisms couple the  
 703 remineralization of sedimentary organic carbon to the reduction of an oxidant (primarily  
 704  $O_2$ ,  $NO_3^-$ ,  $SO_4^{2-}$ , and  $Fe^{3+}$ ; Konhauser, 2007). Thus, a portion of the estimated organic  
 705 carbon loss can be accounted for in the early diagenetic minerals pyrite and siderite,  
 706 which form from microbial dissimilatory sulfate and ferric iron respiration, respectively.  
 707 In the following calculations, we assume the stoichiometry of Fe-(oxyhydr)oxide  
 708 reduction, where one mole of organic carbon is remineralized per four moles of siderite  
 709 produced:



712 and sulfate reduction, where four moles of organic carbon are remineralized per mole of  
 713 pyrite produced:



716 We note that if  $Fe^{2+}$  for pyrite formation were also reduced locally it would require  
 717 additional  $C_{org}$  consumption, akin to Eqn. (3).



718 To correct for the presence of siderite within samples, we relate the measured  
 719 molar quantity of siderite to the Fe<sup>3+</sup> respiration stoichiometries of Eqns. 3 and 4 to  
 720 estimate the necessary weight percent of organic carbon consumed to produce this  
 721 siderite ( $C_{siderite}$ ):

$$722 \quad C_{siderite} = \left( \frac{\left[ \text{measured siderite (mol)} \times \left( \frac{1 \text{ mol } C_{org}}{4 \text{ mol siderite}} \right) \right] \times \gamma}{\text{sample weight (g)}} \right) \times 100 \quad (7)$$

723 where  $\gamma$  converts measured values in moles to wt.%. Likewise, to correct for the presence  
 724 of pyrite, we relate the measured molar quantity of pyrite within each sample to the  
 725 stoichiometry of SO<sub>4</sub><sup>2-</sup> respiration (Eqns. 5 and 6) in order to estimate the weight percent  
 726 of organic carbon remineralized to produce this pyrite ( $C_{pyrite}$ ):

$$727 \quad C_{pyrite} = \left( \frac{\left[ \text{measured pyrite (mol)} \times \left( \frac{4 \text{ mol } C_{org}}{1 \text{ mol pyrite}} \right) \right] \times \gamma}{\text{sample weight (g)}} \right) \times 100 \quad (8)$$

728 Equation (8) does not account for any C<sub>org</sub> consumed to reduce iron for pyrite (e.g., Eqn.  
 729 3). In this regard, Eqns. 8 and 9 conservatively underestimate the weight percent of  
 730 organic carbon remineralized to form pyrite for the case that iron was reduced locally,  
 731 rather than sourced as Fe<sup>2+</sup>.

732 With these estimates, we augment Eqn. (2) as:

$$733 \quad \left( \frac{\hat{C}_{org}^* - (C_{org} + C_{pyrite} + C_{siderite})}{\hat{C}_{org}^*} \right) \times 100 \quad (9)$$

734 This exercise yields a corrected median %  $\hat{C}_{org}^*$  loss for the middle and upper Thornton  
 735 members of 96.2%, not significantly different than the estimate from Eqn. 2 (Fig. 7). In  
 736 contrast, and with the exception of phosphorus-enriched samples in the uppermost  
 737 measured meters, the corrected median loss for the Arthur Creek indicates that there is an

738 excess wt.% of organic carbon to account for the observed wt.% phosphorus (Fig. 7).  
 739 However, the observed quantity of siderite within Thornton and Arthur Creek samples  
 740 may represent a late diagenetic addition to the sediment column and, thus, may not have  
 741 formed through local iron respiration consuming  $C_{org}$ . If this were the case, the %  $C_{org}$   
 742 loss would be less than the value estimated by Eqn. (9), and closer to the value  
 743 determined by Eqn. (2).

744 With sulfate and ferric iron accounted for, the only quantitatively important  
 745 remaining oxidant is molecular oxygen (Konhauser, 2007). In this regard, and if the  
 746 above assumptions hold, the implication is that the majority of the hypothesized organic  
 747 carbon loss was through respiration using molecular oxygen. We define a ratio of the  
 748 estimate of organic matter consumed through anoxic respiration (that is, with  $Fe^{3+}$  and  
 749  $SO_4^{2-}$ :  $C_{siderite}$  and  $C_{pyrite}$ , respectively) to the estimate of  $C_{org}$  loss not accounted for by  
 750 this estimated anoxic remineralization. We calculate the ratio of anoxic to oxic  
 751 respiration as:

$$752 \quad \frac{anoxic}{oxic} \text{ respiration} = \frac{C_{pyrite} + C_{siderite}}{\hat{C}_{org}^* - (C_{org} + C_{pyrite} + C_{siderite})} \quad (10)$$

753 In solving Eqn. (10), we obtain a median (1<sup>st</sup>, 3<sup>rd</sup> quartile) value of 0.02 (0.1, 0.4) for the  
 754 middle and upper Thornton members. This is to say that a median 2% of the estimated  
 755 organic carbon delivery required to source the observed phosphorus content was  
 756 remineralized through anoxic pathways—98% must have been remineralized with  
 757 molecular oxygen to explain the absence of this organic carbon from measured samples.  
 758 If, however, one assumes a diffusive loss of either sulfide or ferrous iron from the  
 759 sediment column (i.e., the numerator underestimates the organic carbon consumed by  
 760 anoxic remineralization), the estimated percent of anoxic remineralization becomes a

761 minimum. If such diffusive loss occurred, then the proportion of  $C_{org}$  remineralized  
762 through oxic respiration would be less than 98% and approach 0% as the sedimentary  
763 production of sulfide and/or  $Fe^{2+}$  through microbial dissimilatory redox reactions  
764 quantitatively consumed  $\hat{C}_{org}^*$ . While we cannot determine the diffusive flux of  
765 reductants from Thornton or Arthur Creek sediments based on preserved geochemical  
766 signals, we note that such a diffusive loss would be possible if the redox boundary  
767 resided within the water column.

768         The calculated weight percent organic carbon required to deliver the observed  
769 phosphorus is notable; the median value, 18.6 wt.%, exceeds organic carbon export to the  
770 sea floor in most modern marine environments (Hedges and Keil, 1995). While such low  
771 organic carbon preservation efficiencies (or, as we describe, high %  $\hat{C}_{org}^*$  loss estimates)  
772 commonly occur within modern marine environments, they typify depositional  
773 environments with low sediment accumulation rates ( $< \sim 0.02$  cm/yr) or oxygenated shelf  
774 settings ( $> 20$   $\mu$ M bottom-water  $O_2$ ; Canfield, 1994; Hedges and Keil, 1995). While we  
775 cannot provide unequivocal evidence that substantial aerobic carbon respiration did not  
776 consume most of the  $C_{org}$  originally delivered to the Thornton sediment column, we  
777 find it difficult to reconcile how such substantial aerobic respiration could have  
778 proceeded without concurrently driving the sediment column anoxic, providing a  
779 negative feedback on the efficiency of organic carbon respiration. Moreover, we note that  
780 the oxidant demand to remineralize this magnitude of organic carbon is difficult to  
781 reconcile with Cambrian oxygen levels, perhaps 15 – 50% present atmospheric  
782 concentrations (Dahl et al., 2010; Bergman et al., 2004; for alternative views, see Berner,  
783 2006; Garrels and Lerman, 1984). Nevertheless, it remains a possibility that episodes of

784 intense aerobic respiration—and efficient capture of released P within authigenic  
785 phases—account for Thornton Limestone phosphatic carbonate precipitation (although  
786 see Föllmi et al. (2005) for discussion of a Miocene phosphogenic episode in which P  
787 sourced from aerobic respiration was ruled out). If, however, one accepts the conclusion  
788 that organic burial alone does not provide an adequate source of phosphorus to the  
789 sediment column, then an additional source of P must have been present during  
790 Thornton deposition.

791         Phosphorus adsorbed onto and/or co-precipitated with metal oxide particles  
792 provides a second potential source of P to the sediment column whose importance  
793 depends, in part, on the magnitude of the flux of metal oxides to the sediment column  
794 (Shaffer, 1986; Feely et al., 1990; Feely et al., 1998; Poulton and Canfield, 2006).  
795 Accordingly, we estimate phosphorus delivery under the assumption of an appreciable  
796 iron-bound P flux, for simplicity based entirely on P adsorbed to iron (oxyhydr)oxides.  
797 This assumption is consistent with the order-of-magnitude calculations presented above;  
798 nonetheless, we acknowledge that other metal oxides, particularly manganese, play an  
799 important role in the cycling of phosphorus (e.g., Dellwig et al., 2010).

800         Ideally, iron-speciation measurements could provide the basis for a quantitative  
801 estimate of Fe-bound P delivered to the sediment column. But before we can perform  
802 such a calculation, we ask whether the  $Fe_{ox}$ ,  $Fe_{mag}$ ,  $Fe_{carb}$ , and  $Fe_{py}$  pools as determined by  
803 iron speciation in carbonate-rich strata of the Thornton Limestone and Arthur Creek  
804 Formation reflect primary depositional reservoirs, or if post-depositional diagenesis could  
805 have converted iron into, out of, or between these phases of the highly reactive iron pool?  
806 Specifically, if these lithologies experienced closed system (with respect to mass)

807 diagenetic remobilization of Fe, then it is likely that appreciable amounts of Fe were  
808 transferred between highly reactive iron phases (e.g., the formation of  $\text{Fe}_{\text{carb}}$  and  $\text{Fe}_{\text{py}}$   
809 through the reduction of an  $\text{Fe}_{\text{ox}}$  precursor phase). In this regard, the value for  $\text{Fe}_{\text{HR}}$  would  
810 still accurately represent the primary iron pool—and could thus be used in calculations of  
811 Fe-bound P delivery—however calculations involving any individual  $\text{Fe}_{\text{HR}}$  phase (e.g.,  
812  $\text{Fe}_{\text{ox}}$ ,  $\text{Fe}_{\text{carb}}$ ) would not provide robust estimates of Fe-bound P. Alternatively, if these  
813 lithologies underwent open system diagenesis, the resulting addition or loss of Fe from  
814 the  $\text{Fe}_{\text{HR}}$  pool (from any and/or all constituent phases) would render *any* calculation based  
815 on the iron speciation data suspect. While we cannot eliminate the possibility of Fe  
816 addition during open system diagenesis, we note that Fe-speciation data for the  
817 Thornton Limestone and Arthur Creek Formation are consistent with other redox  
818 proxies (see above) favoring the view that the highly reactive iron species in these rocks  
819 record a substantial depositional flux.

820         In the following discussion we provide a methodology to address the potential  
821 contribution of the Fe-P shuttle to Thornton and Arthur Creek sediments under the  
822 assumption of limited or closed system iron diagenesis. To this end, we employ iron  
823 speciation data from these lithologies for illustrative calculations. These calculations  
824 provide a consistency argument given that organic-bound P was likely insufficient to  
825 account for the measured P content. Throughout this discussion, we introduce and  
826 emphasize the caveats inherent to the use of a diagenetically mobile element in these  
827 calculations.

828         The molar ratio of the co-precipitation of phosphorus onto iron (oxyhydr)oxide  
829 particles conforms to a distribution coefficient ( $K_D$ ) model that scales linearly to the

830 ambient seawater phosphate concentration ( $[P_{sw}]$ ) (Feely et al., 1991; 1998; Konhauser et  
831 al., 2007):

$$832 \quad \left( \frac{P}{Fe} \right)_{molar} = K_D \times [P_{sw}]. \quad (11)$$

833 Thus, to estimate the delivery of iron-bound phosphorus,  $\hat{P}_{Fe}^*$ , we multiply an estimate of  
834 iron oxide delivery ( $\hat{F}e_{ox}^*$ ) by the adsorption coefficient of phosphorus to iron oxides  
835 ( $K_D$ ) for a given estimate of seawater phosphate concentration ( $[P_{sw}]$ ):

$$836 \quad \hat{P}_{Fe}^* = \gamma \hat{F}e_{ox}^* \times K_D \times [P_{sw}] \quad (12)$$

837 where  $\gamma$  converts measured values (in wt.%) to moles as required in the definition of the  
838 adsorption coefficient. Within anoxic pore-waters, a fraction of the iron oxides delivered  
839 to the sediment column will be reduced by dissimilatory iron reduction and converted to  
840 ferrous iron, and these ions will either precipitate as pyrite or iron carbonate, or  
841 advect/diffuse to the overlying water column. Accordingly, a full accounting of  $\hat{F}e_{ox}^*$   
842 would include all of these conservation and loss terms. The estimate would become a  
843 lower bound on  $\hat{P}_{Fe}^*$  if we ignored the ferrous iron loss flux, which in any event is  
844 unconstrained, and included only the measured iron oxide ( $Fe_{ox}$ ), pyrite ( $Fe_{py}$ ) and iron-  
845 carbonate phases ( $Fe_{carb}$ ). We note, however, that at least some of the measured Fe (most  
846 obviously the  $Fe_{carb}$  phase) may have originated from diagenetic remobilization of iron to  
847 these carbonates. (For the lower Thornton Limestone,  $Fe_{carb}$  comprises a median (1<sup>st</sup>, 3<sup>rd</sup>  
848 quartile) of 76.8 % (71.3, 81.8) of the total iron pool; in contrast, for the phosphatic  
849 middle/upper Thornton and for the Arthur Creek Formation,  $Fe_{carb}$  accounts for only

850 28.7 % (22.3, 33,2) and 20 % (15.15, 23.5) of  $Fe_T$ , respectively.) In this regard, this  
851 calculation may overestimate  $\hat{P}_{Fe}^*$ .

852 Magnetite may form through the reductive dissolution of mixed ferrous–ferric  
853 oxide phases (e.g., Zegeye et al., 2012), and, as such, could be considered in the  
854 summation of primary iron oxide minerals ( $\hat{F}e_{ox}^*$ ); however, magnetite may also form  
855 during prograde metamorphism, in which case inclusion of this phase would over-  
856 estimate the primary ferric iron flux to the sediment column. We include  $Fe_{mag}$  within our  
857 calculation because the authigenic pathway likely exceeds weathering and metamorphic  
858 overprints for this depositional environment. (Regardless, within NTGS 99/1 magnetite  
859 represents a negligible component of  $Fe_T$ , therefore this assumption does not alter the  
860 illustrative estimate for  $\hat{P}_{Fe}^*$ .) Therefore, we rewrite Eqn (12) in the approximate form:

$$861 \quad \hat{P}_{Fe}^* = \gamma(Fe_{ox} + Fe_{py} + Fe_{carb} + Fe_{mag}) \times K_D \times [P_{SW}]. \quad (13)$$

862 A host of seawater ions—notably silica, trace metals and rare earth elements—  
863 compete with phosphorus for adsorption sites on the surface of iron oxide particles (e.g.,  
864 Berner, 1973; Trocine and Trefry, 1988; Olivarez and Owen, 1989; Trefry and Metz,  
865 1989; Feely et al., 1991; Feely et al., 1998; German et al., 1990; Konhauser et al., 2007).  
866 Thus, the choice of  $K_D$  depends on the assumption of the seawater composition of  
867 Cambrian oceans. As these element concentrations are broadly unknown for the  
868 Paleozoic Era, we focus here only on the role of the major seawater constituent dissolved  
869 silica in competition for iron-surface anion sites. Following Siever’s (1992) inference of  
870 cristobalite saturation for early Phanerozoic seawater ( $[Si_{SW}] = 0.67$  mM), Konhauser et  
871 al. (2007) determined experimentally a  $K_D = 0.0108$  for ferrihydrite at this silica  
872 saturation state. Notably, the linear range of the  $K_D$  model depends on the phosphorus

873 concentration of ambient seawater. At cristobalite saturation, the linearity of the  $K_D$   
874 model saturates above  $\sim 5 \mu\text{M}$   $[\text{P}_{\text{sw}}]$ . This is to say that the co-precipitation and delivery of  
875 phosphorus bound to iron oxides remains constant at and above this ambient seawater  
876 phosphate concentration.

877 Hence, we adopt  $[\text{P}_{\text{sw}}] = 5 \mu\text{M}$  to calculate a maximum estimate for  $\hat{P}_{\text{Fe}}^*$  at the  
878 adopted  $[\text{Si}_{\text{sw}}]$ . We emphasize that the chosen value of  $5 \mu\text{M}$  is a simplistic assumption  
879 and that water column phosphorus concentrations are affected by variable environmental  
880 factors that are difficult to generalize, even under well-constrained modern conditions.  
881 Nevertheless, this adopted phosphate concentration is consistent with modern anoxic  
882 environments, including the Black Sea and Cariaco Basin (Shaffer, 1986; Scranton et al.,  
883 2006). For example, in the Black Sea, higher phosphate concentrations in the ferruginous  
884 chemocline than in the underlying sulfidic waters result from the dissolution of settling  
885 Fe-oxides and the release of adsorbed phosphate (Brewer and Murray, 1973). Similar  
886 processes are suggested to explain the phosphate concentrations (up to  $9 \mu\text{M}$  dissolved P)  
887 in the ferruginous Lake Matano (Crowe et al., 2008) where the release of Fe(III)-bound P  
888 at the chemocline is balanced by the precipitation of Fe(II)-phosphates below the  
889 chemocline.

890 Applying Eqn. (13) to samples from the middle and upper Thornton members  
891 yields a median estimate for iron-bound P of 0.1 wt.% as compared to a median estimate  
892 of 0.2 wt.% for the Arthur Creek (Fig. 7). In this formulation, phosphorus delivery by  
893 iron oxides is proportional to the highly reactive iron phases ( $\text{Fe}_{\text{HR}}$ ) determined from iron  
894 speciation geochemistry. While  $\text{Fe}_{\text{HR}}/\text{Fe}_{\text{T}}$  decreases between the P-enriched middle /  
895 upper Thornton members and the Arthur Creek, the observed increase in  $\text{Fe}_{\text{T}}$  within the



896 Arthur Creek compensates such that the molar estimate of  $\hat{F}_{e_{ox}}^*$ , and, thus,  $\hat{P}_{Fe}^*$  remains  
897 roughly constant between the two formations. As such, and if the above assumptions  
898 hold, this implies that the relative contribution of the Fe-P shuttle to the observed weight  
899 percent sedimentary P was much greater during deposition of the Arthur Creek Formation  
900 because of the lower wt.%  $P_T$  measured throughout this formation. Indeed, the median  
901 estimate of  $\hat{P}_{Fe}^* = 0.2$  wt.% for the Arthur Creek greatly exceeds the median measured  $P_T$   
902 (0.03 wt.%; Fig. 7). In contrast, the median estimate of  $\hat{P}_{Fe}^* = 0.1$  wt.% for the middle and  
903 upper Thornton members provides only ~10% of the median measured  $P_T$  (0.98 wt.%;  
904 Fig. 7), and proportionally less for samples with the highest measured  $P_T$  approaching 4  
905 wt.%. Likewise, any diffusive loss of P from the sediment column prior to lithification  
906 would increase the requisite  $\hat{P}_{Fe}^*$  and, in the case of the Thornton, increase the  
907 deficiency between the observed  $P_T$  and P hypothesized to have been delivered associated  
908 with  $Fe_{ox}$  ( $\hat{P}_{Fe}^*$ ).

909 The formulation of our equations may significantly overestimate Fe-bound P  
910 delivery for two reasons. First, our calculations adopt a  $K_D$  value based on an estimate of  
911 contemporaneous seawater silica concentrations. Second, our calculations adopt a  
912 seawater phosphate concentration that maximizes the potential for phosphorus delivery  
913 by the iron shuttle. If we presumed a higher seawater silica concentration (that is,  
914 decreased  $K_D$ ), or if, for an assumed  $[Si_{SW}]$ , we also assumed a lower  $[P_{SW}]$ , then we  
915 would calculate a lower P delivery flux per unit  $Fe_{ox}$ . Thus, both of these changes would  
916 yield a lower estimate of  $\hat{P}_{Fe}^*$  for a given iron flux to the sediment column.

917           Some iron minerals are more effective P delivery shuttles than others. The  
918 capacity for iron minerals to scavenge and deliver phosphorus to the sea floor depends on  
919 a number of factors, including the surface density of adsorption sites, which in part is  
920 related to mineral surface area. In this regard, amorphous to poorly crystalline phases will  
921 scavenge more phosphate than highly crystalline phases. (We note, however, that  
922 progressive crystallization may result in the subsequent desorption of P from adsorption  
923 sites. If this desorption occurs within the sediment column, outside the length-scales of  
924 advection/diffusion with the overlying water-column, Fe-bound P could provide a  
925 significant source of P to the sediment column.) Here we assumed ferrihydrite as the  
926 carrier phase (Konhauser et al., 2007), however, a range of other iron minerals form  
927 during anaerobic  $\text{Fe}^{2+}$  oxidation (e.g., Kappler and Newman, 2004; Zegeye et al., 2012).  
928 For instance, in the only detailed study of Fe mineralogy in a ferruginous water column  
929 (Lake Matano, Indonesia), Zegeye et al. (2012) found that ferrihydrite was quantitatively  
930 transformed to carbonated green rust ('fougerite') during settling through the water  
931 column, with more minor formation of magnetite. Unfortunately, no experimental data  
932 currently exist for P adsorption to green rust under the chemical conditions likely  
933 encountered in Cambrian oceans (e.g., Lake Matano has relatively low [Si]). However,  
934 adsorption of oxyanions to green rust tends to be far higher than for ferrihydrite (Randall  
935 et al., 2001), and thus such a finding highlights the need to consider multiple and varied  
936 carrier phases for the ancient Fe-P shuttle. An iron carrier phase with an adsorption  
937 coefficient ( $K_D$ ) with respect to P greater than ferrihydrite could have delivered more P to  
938 Thornton sediments for a given iron flux to the sea floor.

939 Are there other scenarios in which the delivery of Fe-bound P could have been  
940 greater than that inferred from the formulations of equations 11 through 13? To answer  
941 this question it is necessary to address whether the measured  $Fe_{HR}$  is an accurate proxy  
942 for the contribution of  $Fe_{ox}$  to the sediment column, or whether it could underestimate the  
943 original  $Fe_{ox}$  flux ( $\hat{F}e_{ox}^*$ ), and, thus,  $\hat{P}_{Fe}^*$  to the sediment column. Next, we explore  
944 hypothetical redox scenarios in which Fe-bound P could contribute more substantially to  
945 authigenic apatite. Without an independent line of evidence that the constituent phases of  
946 the highly reactive iron pool represent the primary fluxes of iron to the sediment column,  
947 we choose not to advocate for this possibility for the Thornton Limestone.  
948 Nevertheless, with regard to the broader question of the mechanism for phosphatic  
949 carbonate deposition, we find it informative to evaluate the circumstances in which the  
950 Fe-bound delivery shuttle could contribute substantially to phosphogenesis and  
951 phosphatic carbonate deposition.

952 One can envision a spectrum of scenarios for the relative magnitudes of  $Fe_{ox}$   
953 delivery to and  $Fe^{2+}$  loss from the sediment column. These scenarios fall within three  
954 generalized categories:  $Fe_{ox}$  delivery (1) greater than, (2) nearly equal to, or (3) less than  
955  $Fe^{2+}$  diffusive/advective loss. In the following discussion we discount scenario (3)  
956 because such an imbalance defines an unsustainable Fe cycle. To begin, we consider the  
957 scenario that (1)  $Fe_{ox}$  delivery exceeds  $Fe^{2+}$  loss. This can result from two opposing redox  
958 regimes. (1a) If the majority of  $Fe_{ox}$  delivered to the sediment column were stabilized  
959 within oxygenated pore-water then this would preclude widespread iron reduction. In this  
960 instance, only a small amount P would be liberated from the  $Fe_{ox}$  delivery shuttle, and  
961  $Fe_{ox}$  would dominate  $Fe_{HR}$ . (1b) Alternatively, if sedimentary electron donors (e.g.,  $C_{org}$ )

962 contributed to pore-water anoxia, some fraction of the delivered  $\text{Fe}_{\text{ox}}$  would be reduced to  
963  $\text{Fe}^{2+}$ , and any P bound to these  $\text{Fe}_{\text{ox}}$  particles would be released to pore-waters. To  
964 maintain the low  $\text{Fe}^{2+}$  loss fraction defining this scenario, any  $\text{Fe}^{2+}$  ions produced must be  
965 captured quantitatively within authigenic ferrous iron minerals. In this instance,  
966 sedimentary Fe would be partitioned amongst  $\text{Fe}_{\text{ox}}$ ,  $\text{Fe}_{\text{carb}}$ , and  $\text{Fe}_{\text{py}}$  phases, and the  
967 dominance of the latter two minerals would imply that much of the original  $\text{Fe}_{\text{ox}}$  flux was  
968 reduced. Notably, with regard to P delivery, either scenario for high  $\text{Fe}_{\text{ox}}$  delivery relative  
969 to  $\text{Fe}^{2+}$  loss predicts that the measurement of sedimentary  $\text{Fe}_{\text{HR}}$  represents a close  
970 approximation of the magnitude of P delivery associated with the Fe-P shuttle ( $\hat{P}_{\text{Fe}}^*$ ). If,  
971 for example, the Fe cycle were operating in this manner at the time of deposition of the  
972 middle and upper Thornton members then, under the above assumptions, the Fe-shuttle  
973 would be constrained to have contributed a median of  $\sim 10\%$   $\text{P}_T$  (as determined from Eqn.  
974 13) and, therefore, could not represent a dominant source of P for the observed  
975 enrichment.

976         If scenarios 1a and 1b cannot source significant amounts of Fe-bound P to  
977 phosphatic lithologies, can scenario 2? Like scenario (1b) above, scenario (2) necessitates  
978 a redox environment that facilitates the reductive dissolution of the majority of  $\text{Fe}_{\text{ox}}$   
979 delivered to the sediment column, regardless of the size of this flux. In contrast, scenario  
980 (2) is distinguished from scenario (1) by the condition that the majority of the  
981 sedimentary  $\text{Fe}^{2+}$  produced must escape to the overlying water column, resulting in less  
982 capture of  $\text{Fe}^{2+}$  ions in authigenic minerals. Such diffusive loss requires anoxia within the  
983 water-mass overlying the sediment column. As above, Fe retained within the sediment  
984 can reside in any combination of  $\text{Fe}_{\text{ox}}$ ,  $\text{Fe}_{\text{carb}}$ , and/or  $\text{Fe}_{\text{py}}$  phases. Notably, Scenario (2)

985 allows for the measured  $Fe_{HR}$  value to significantly underestimate iron oxide delivery to  
986 the sea floor ( $\hat{F}e_{ox}^*$ ) and, therefore, to underestimate the Fe-P shuttle ( $\hat{P}_{Fe}^*$ ). If, for  
987 example, the Fe cycle were operating with an extensive benthic flux of  $Fe^{2+}$  to the water  
988 column during deposition of the middle Thornton Limestone, and if a mechanism  
989 existed to preferentially retain the delivered P, then the Fe-P shuttle could have provided  
990 a significant proportion of the observed P to these phosphatic strata, that is, greater than  
991 the ~10% estimated from Eqn. (13).

992 In summary, simple models of Fe-bound P delivery estimates ( $\hat{P}_{Fe}^*$ ), as determined  
993 from Eqn. (13), indicate that this delivery shuttle could have sourced the measured P  
994 content of the Arthur Creek Formation. In contrast, our estimates of Fe-bound P can only  
995 account for a median of 10% of the P content the Thornton Limestone. (This estimate  
996 assumes that  $Fe_{HR}$  in Thornton rocks reflects deposition from the water column. To the  
997 extent that Thornton iron minerals reflect open-system diagenesis, this estimate would  
998 be even lower.) Only by invoking a major diffusive loss of iron from the Thornton  
999 sediment column with subsequent capture of delivered P within authigenic phases—a  
1000 scenario for which we do not advocate, yet do not find inconsistent with the assumption  
1001 of limited diagenesis—could Fe-bound P have provided a more substantial contribution  
1002 to phosphatic carbonates of the Thornton Limestone.

1003

## 1004 CONCLUSIONS

1005 Within drill core NTGS 99/1, phosphorus enrichment is confined to the middle  
1006 and upper members of the Thornton Limestone, and petrographic observations reveal  
1007 that this enrichment reflects authigenic apatite mineral nucleation primarily associated

1008 with the interior of bioclasts and, more rarely, as cement in bioclastic grainstone. Under  
1009 the canonical model that phosphorus bound within organic matter represents the only  
1010 significant delivery flux of phosphorus to the sediment column, molar  $C_{\text{org}}:P_{\text{T}}$  well below  
1011 the Redfield ratio requires significant  $C_{\text{org}}$  loss or a second delivery source of phosphorus  
1012 to Thornton sediments.

1013         Interpreted together, sedimentological observations and iron speciation data  
1014 suggest that sediment within the southern Georgina Basin accumulated under anoxic,  
1015 ferruginous conditions. This redox diagnosis is consistent with previous research  
1016 documenting the propensity for anoxic, ferruginous conditions in subsurface water  
1017 masses of late Neoproterozoic and Cambrian oceans (Canfield et al., 2008) driven by the  
1018 relative fluxes of electron donors (organic carbon) and electron acceptors (reactive Fe,  
1019 sulfate) into a basin (Johnston et al., 2010). If correct, the conclusion of an active iron  
1020 redox cycle contemporaneous with the deposition of the Thornton Limestone and  
1021 Arthur Creek Formation provides a second mechanism for augmented sedimentary  
1022 phosphorus delivery—phosphorus adsorbed to particulate iron minerals.

1023         The stoichiometries of delivery estimates and remineralization reactions indicate  
1024 that the phosphorus content of the Arthur Creek Formation is easily accounted for by any  
1025 combination of phosphorus associated with organic matter and/or iron oxide fluxes.  
1026 However, the observed phosphorus content of the Thornton is difficult to reconcile with  
1027 reasonable fluxes of either organic-bound or iron-bound phosphorus alone. Thus, we  
1028 suggest that both sources were necessary to account for Thornton Limestone phosphatic  
1029 carbonate deposition.

1030           The discontinuous nature of phosphorite and phosphatic carbonate through Earth  
1031 history speaks to discontinuous mechanisms of formation. We hypothesize that redox-  
1032 mediated phosphorus delivery via the Fe-P shuttle, rather than a discontinuous organic  
1033 carbon flux, provides the more intermittent mechanism for phosphorus delivery to the  
1034 sediment column. That said, ferruginous bottom waters appear to have been widespread  
1035 in Proterozoic oceans, whereas phosphatic carbonates are not. Thus, the episodic nature  
1036 of phosphate deposition must additionally depend on the fate of phosphate after it enters  
1037 the sediment column. Where the oxic-anoxic interface lies well within the water column,  
1038 microbial reduction of ferric iron within the sediments will remobilize P, with a high  
1039 probability of escape back to the water column. Where phosphate in solution is trapped  
1040 by skeletons, however, or bound to decay-resistant materials such as chitinous  
1041 exoskeletons, mineral phosphate may be reprecipitated in sediments. With this in mind,  
1042 it would appear that delivery mechanisms, post-delivery fate within sediments, and  
1043 evolution all contributed to the observed geological record of Cambrian phosphate  
1044 accumulation.

1045

#### 1046 **ACKNOWLEDGMENTS**

1047 We thank the Northern Territory Geological Survey and Max Heckenberg and Jay Carter  
1048 of the Alice Springs Core Library for generous access to core material. The Agouron  
1049 Institute and the NASA Astrobiology Institute (MIT node) provided financial support.  
1050 We thank Paul Myrow for discussions of sedimentology, Eric Morrow for assistance with  
1051 data analysis, Greg Eiseheid for technical support in the Harvard University Laboratory  
1052 for Geochemical Oceanography, and David Fike and an anonymous reviewer for critical  
1053 comments that helped to improve this paper.

1054

1055 **REFEENCES CITED**

- 1056 Algeo, T.J., and Ingall, E., 2007, Sedimentary C<sub>org</sub>:P ratios, paleocean ventilation, and  
1057 Phanerozoic atmospheric pO<sub>2</sub>: *Palaeogeography, Palaeoclimatology, Palaeoecology* v. p.  
1058 130–155, doi:10.1016/j.palaeo.2007.02.029.  
1059
- 1060 Ambrose, G., and Putnam, P., 2006, The Georgina Basin 2006: Northern Territory of  
1061 Australia onshore hydrocarbon potential: Northern Territory Geological Survey, Record  
1062 2006-003.  
1063
- 1064 Ambrose G.J., Kruse P.D., and Putman P.E., 2001, Geology and hydrocarbon potential of  
1065 the southern Georgina Basin, Australia: *Australian Petroleum Production and Exploration*  
1066 *Association Journal*, v. 41, p. 139–163.  
1067
- 1068 Anderson L. D., Delaney M. L. and Faul K. L., 2001, Carbon to phosphorus ratios in  
1069 sediments: implications for nutrient cycling: *Global Biogeochemical Cycles*, v. 15, p. 65–  
1070 79, doi:10.1029/2000GB001270.  
1071
- 1072 Anderson, T.F., and Raiswell, R., Sources and mechanisms for the enrichment of highly  
1073 reactive iron in euxinic Black Sea sediments: *American Journal of Science*, v. 304, p.  
1074 203-233, doi:10.2475/ajs.304.3.203.  
1075
- 1076 Babcock, L.E., and Shanchi Peng, 2007, Cambrian chronostratigraphy: Current state and  
1077 future plans: *Palaeogeography, Palaeoclimatology, Palaeoecology*, v. 254, p. 62–66,  
1078 doi:10.1016/j.palaeo.2007.03.011.  
1079
- 1080 Bartley, J.K., Pope, M., Knoll, A.H., Semikhatov, M.A., and Petrov, P.Yu., 1998, A  
1081 Vendian—Cambrian boundary succession from the northwestern margin of the Siberian  
1082 Platform: stratigraphy, palaeontology, chemostratigraphy and correlation: *Geological*  
1083 *Magazine*, v. 135, p. 473-494, doi:10.1017/S0016756898008772.  
1084
- 1085 Baturin, G. N., and Bezrukov, P. L., 1979, Phosphorites on the sea floor and their origin:  
1086 *Marine Geology*, v. 31, p. 317–332, doi: 10.1016/0025-3227(79)90040-9.  
1087
- 1088 Bengtson, S., and Yue Zhao, 1997, Fossilized metazoan embryos from the earliest  
1089 Cambrian: *Science*, v. 277, p. 1645-1648, doi:10.1126/science.277.5332.1645.  
1090
- 1091 Bengtson, S., Conway Morris, S., Cooper, B.J., Jell, P.A., and Runnegar, B.N., 1990,  
1092 Early Cambrian Fossils from South Australia: *Memoirs of the Association of*  
1093 *Australasian Palaeontologists*, v. 9, p. 1-364.  
1094
- 1095 Benitez-Nelson, C.R., 2000, The biogeochemical cycling of phosphorus in marine  
1096 systems: *Earth-Science Reviews*, v. 51, p. 109-135, doi: 10.1016/S0012-  
1097 82252(00)00018-0.  
1098



1099 Bergman, N.M., Lenton, T.M., and Watson, A.J., 2004, COPSE: A new model of  
1100 biogeochemical cycling over Phanerozoic time: *American Journal of Science*, v. 304, p.  
1101 397-437, doi: 10.2475/ajs.304.5.397.  
1102  
1103 Berner, R. A., 1973, Phosphate removal from sea water by adsorption on volcanogenic  
1104 ferric oxides: *Earth and Planetary Science Letters*, v. 18, p. 77–86, doi: 10.1016/0012-  
1105 821X(73)90037-X.  
1106  
1107 Berner, R.A., 2006, GEOCARBSULF: A combined model for Phanerozoic atmospheric  
1108 O<sub>2</sub> and CO<sub>2</sub>: *Geochimica et a Cosmochimica Acta*, v. 70, p. 5653-5664, doi:  
1109 10.1016/j.gca.2005.11.032.  
1110  
1111 Bjerrum, C.J., and Canfield, D.E., 2002, Ocean productivity before about 1.9 Gyr ago  
1112 limited by phosphorus adsorption onto iron oxides: *Nature*, v. 417 p. 159–162,  
1113 doi:10.1038/417159a.  
1114  
1115 Boreham, C.J., and Ambrose, G.J., 2005, Cambrian petroleum systems in the southern  
1116 Georgina Basin, Northern Territory, Australia, *Central Australian Basins Symposium:*  
1117 *petroleum and minerals potential*, Alice Springs, NT, 16–18 August 2005.  
1118  
1119 Brewer, P.G., and Murray, J.W., 1973, Carbon, nitrogen and phosphorus in the Black  
1120 Sea: *Deep-Sea Research*, v. 20, p. 803-818.  
1121  
1122 Brasier, M.D., and Callow, R.H.T., 2007, Changes in the Patterns of Phosphatic  
1123 Preservation across the Proterozoic-Cambrian Transition: *Memoirs of the Association of*  
1124 *Australasian Palaeontologists*, No. 34, p. 377-389.  
1125  
1126 Butterfield, N.J., 2003, Exceptional fossil preservation and the Cambrian explosion:  
1127 *Integrative and Comparative Biology*, v. 43, p. 166–177, doi: 10.1093/icb/43.1.166.  
1128  
1129 Canfield, D.E., 1994, Factors influencing organic carbon preservation in marine  
1130 sediments: *Chemical Geology*, v. 114 p. 315–329, doi: 10.1016/0009-2541(94)90061-2.  
1131  
1132 Canfield, D.E., Lyons, T.W., and Raiswell, R., 1996, A model for iron deposition to  
1133 euxinic Black Sea sediments: *American Journal of Science*, v. 296, p. 818–834.  
1134  
1135 Canfield, D.E., Poulton, S.W., Knoll, A.H., Narbonne, G.M., Ross, G., Goldberg, T., and  
1136 Strauss, H., 2008, Ferruginous conditions dominated later Neoproterozoic deep-water  
1137 chemistry: *Science*, v. 321, p. 949-952, doi: 10.1126/science.1154499.  
1138  
1139 Canfield D. E., Raiswell R. and Bottrell S., 1992, The reactivity of sedimentary iron  
1140 minerals towards sulfide: *American Journal of Science* v. 292, p. 659– 683. Canfield D. E.,  
1141 Raiswell R., Westrich J. T., Reaves C. M. and Berner R. A., 1986, The use of chromium  
1142 reduction in the analysis of reduced inorganic sulfur in sediments and shales: *Chemical*  
1143 *Geology*, v. 54, p., 149–155, doi: 10.1016/0009-2541(86)90078-1.  
1144

1145 Clark, L.L., Ingall, E.D., and Benner, R., 1998, Marine phosphorus is selectively  
1146 remineralized: *Nature*, v. 393, p. 426-426 doi:10.1038/30881.  
1147  
1148 Cook, P.J., 1992, Phosphogenesis around the Proterozoic-Phanerozoic transition: *Journal*  
1149 *of the Geological Society of London*, v. 149, p. 615-620, doi: 10.1144/gsjgs.149.4.0615  
1150  
1151 Cook, P.J., and McElhinny, M.W., 1979, A re-evaluation of the spatial and temporal  
1152 distribution of sedimentary phosphate deposits in the light of plate tectonics: *Economic*  
1153 *Geology and the Bulletin of the Society of Economic Geologists*, v. 74, p. 315–330, doi:  
1154 10.2113/gsecongeo.74.2.315.  
1155  
1156 Cook, P., and Shergold, J.H., 1984, Phosphorus, phosphorites and skeletal evolution at  
1157 the Precambrian–Cambrian boundary: *Nature* v.10, p. 231–236, doi: 10.1038/308231a0.  
1158  
1159 Cook, P.J., and Shergold, J.H., 1986, Proterozoic and Cambrian phosphorites – nature  
1160 and origin: *in* Cook, P.J., and Shergold, J.H., eds., *Phosphate deposits of the world:*  
1161 *Proterozoic and Cambrian phosphorites, Volume 1: Cambridge, UK, Cambridge*  
1162 *University Press*, p. 369-386.  
1163  
1164 Cook, P.J., Shergold, J.H., Burnett, W.C., and Riggs, S.R., 1990, Phosphorite research: a  
1165 historical overview: *Geological Society, London, Special Publication*, v. 52, p. 1-22, doi:  
1166 10.1144/GSL.SP.1990.052.01.02.  
1167  
1168 Cordell, D., Drangert, J.-O., and White, S., 2009, The story of phosphorus: Global food  
1169 security and food for thought: *Global Environmental Change*, v. 19, p. 292-305, doi:  
1170 10.1016/j.gloenvcha.2008.10.009.  
1171  
1172 Crowe, S.A., O'Neill, A.H., Katsev, S., Hehanussa, P., Haffner, G.D., Sundby, B., Mucci,  
1173 A. and Fowle, D.A., 2008, The biogeochemistry of tropical lakes: a case study from Lake  
1174 Matano, Indonesia: *Limnology and Oceanography*, v. 53, p. 319-331.  
1175  
1176 Dahl, T.W., Hammarlund, E.U., Anbar, A.D., Bond, D.P.G., Gill, B.C., Gordon, G.W.,  
1177 Knoll, A.H., Nielsen, A.T., Schovsbo, N.H., Canfield, D.E., 2010, Devonian rise in  
1178 atmospheric oxygen correlated to the radiations of terrestrial plants and large predatory  
1179 fish, v. 107, p. 17911-17915, doi: 10.1073/pnas.1011287107.  
1180  
1181 Delaney M.L., 1998, Phosphorus accumulation in marine sediments and the oceanic  
1182 phosphorus cycle: *Global Biogeochemical Cycles*, v. 12, p. 563–572,  
1183 doi:10.1029/98GB02263.  
1184  
1185 Dellwig, O., Leipe, T., März, C., Glockzin, M., Pollehne, F., Schnetger, B., Yakushev,  
1186 E.V., Böttcher, M.E., and Brumsack, H.-J., 2010, A new particulate Mn-Fe-P-shuttle at  
1187 the redoxcline of anoxic basins: *Geochimica et Cosmochimica Acta*, v. 74, p. 7100-7115.  
1188  
1189 Donoghue, P., Kouchinsky, A., Waloszek, D., Bengtson, S., Dong, X.-p., Val'kov, A.K.,  
1190 Cunningham, J.A., and Repetski, J.E., 2006, Fossilized embryos are widespread but the

1191 record is temporally and taxonomically biased: *Evolution & Development*, v. 8, p. 232–  
1192 238, doi: 10.1111/j.1525-142X.2006.00093.x.

1193

1194 Dornbos, S.Q., Botjer, D.J., Chen, J.-Y., Gao, F., Oliveri, P., and Li, C.-W., 2006,  
1195 Environmental controls on the taphonomy of phosphatized animals and animal embryos  
1196 from the Neoproterozoic Doushantuo Formation, southwest China: *Palaios*, v. 21, p. 3-14,  
1197 doi: 10.2110/palo.2004.p04-37.

1198

1199 Dunster, J.N., Kruse, P.D., Duffett, M.L., and Ambrose, G.J., 2007, Geology and  
1200 resource potential of the southern Georgina Basin: Northern Territory Geological Survey,  
1201 Digital Information Package DIP007.

1202

1203 Feely, R.A., Trefry, J.H., Massoth, G.J., and Metz, S., 1991, A comparison of the  
1204 scavenging of phosphorus and arsenic from seawater by hydrothermal iron  
1205 oxyhydroxides in the Atlantic and Pacific Oceans: *Deep Sea Research*, v. 38, p., 617-623,  
1206 doi: 10.1016/0198-0149(91)90001-V.

1207

1208 Feely, R.A., Trefry, J.H., Lebon, G.T., and German, C.R., 1998, The relationship  
1209 between P/Fe and V/Fe ratios in hydrothermal precipitates and dissolved phosphate in  
1210 seawater: *Geophysical Research Letters*, v. 25, p. 2253-2256, doi:10.1029/98GL01546.

1211

1212 Filippelli, G.M., 2011, Phosphate rock formation and marine phosphorus geochemistry:  
1213 the deep time perspective: *Chemosphere*, v. 84, p. 759-766, doi:  
1214 10.1016/j.chemosphere.2011.02.019.

1215

1216 Filippelli, G.M., and Delaney, M.L., 1992, Similar phosphorus fluxes in ancient  
1217 phosphorite deposits and a modern phosphogenic environment: *Geology*, v. 20, p. 709-  
1218 712, doi: 10.1130/0091-7613(1992)020<070.

1219

1220 Föllmi, K.B., 1996, The phosphorus cycle, phosphogenesis and marine phosphate-rich  
1221 deposits: *Earth-Science Reviews*, v. 40, p. 55–124, doi: 10.1016/0012-8252(95)00049-6.

1222

1223 Föllmi, K.B., Badertscher, C., de Kaenel, E., Stille, P., John, C. M., Adatte, T., and  
1224 Steinmann, P, 2005), Phosphogenesis and organic-carbon preservation in the Miocene  
1225 Monterey Formation at Naples Beach, California—The Monterey hypothesis revisited:  
1226 *Geological Society of America Bulletin*, v. 117, p. 589-619, doi:10.1130/B25524.1.

1227

1228 Garrels, R.M., and Lerman, A., 1984, Coupling of the sedimentary sulfur and carbon  
1229 cycles; an improved model: *American Journal of Science*, v. 284, p. 989-1007, doi:  
1230 10.2475/ajs.284.9.989.

1231

1232 Geider, R., and La Roche, J., 2002, Redfield revisited: variability of C:N:P in marine  
1233 microalgae and its biochemical basis: *European Journal of Phycology*, v. 37, p. 1-17,  
1234 doi:10.1017/S0967026201003456.

1235

1236 German, C.R., Klinkhammer, G.P., Edmond, J.M., Mitra, A., and Elderfield, H., 1990,

- 1237 Hydrothermal scavenging of rare earth elements in the ocean: *Nature*, v. 345, p. 516–518,  
1238 doi:10.1038/345516a0.
- 1239 Gomez, F.J., Ogle, N., Astini, R.A., and Kalin, R.M., 2007, Paleoenvironmental and  
1240 Carbon-Oxygen Isotope Record of Middle Cambrian Carbonates (La Laja Formation) in  
1241 the Argentine Precordillera: *Journal of Sedimentary Research*, v. 77, p. 826-842, doi:  
1242 10.2110/jsr.2007.079.
- 1243 Guo, H., Du, Y., Kah, L.C., Huang, J., Hu, C., Huang, H. and Yau, W., 2013, Isotopic  
1244 composition of organic and inorganic carbon from the Mesoproterozoic Jixian Group,  
1245 North China: Implications for biological and oceanic evolution: *Precambrian Research*, v.  
1246 224, p. 169-183, doi: 10.1016/j.precamres.2012.09.023.
- 1247 Guo, Q., Strauss, H., Liu, C., Zhao, Y., Yang, X., Peng, J., and Yang, H., 2010, A  
1248 negative carbon isotope excursion defines the boundary from Cambrian Series 2 to  
1249 Cambrian Series 3 on the Yangtze Platform, South China: *Palaeogeography,*  
1250 *Palaeoclimatology, Palaeoecology*, v. 285, p. 143–151, doi:10.1016/j.palaeo.2009.11.005.
- 1251 Howard, P.F., 1990, The distribution of phosphatic facies in the Georgina, Wiso and Daly  
1252 River Basins, Northern Australia: Geological Society, London, Special Publications, v.  
1253 52, p. 261-272, doi: 10.1144/GSL.SP.1990.052.01.19
- 1254 Hedges, J.I., and Kiel, R.G., 1995, Sedimentary organic matter preservation: an  
1255 assessment and speculative synthesis: *Marine Chemistry*, v. 49, p.81-115, doi:  
1256 10.1016/0304-4203(95)00008-F.
- 1257 Holland, H.D., 2006, The oxygenation of the atmosphere and oceans: *Philosophical*  
1258 *Transactions of the Royal Society–B*, v. 361, p. 903-915, doi: 10.1098/rstb.2006.1838.  
1259
- 1260 Ingall, E.D., Bustin, R.M., and Van Cappellen, P., 1993, Influences of water column  
1261 anoxia on the burial and preservation of carbon and phosphorus in marine shales:  
1262 *Geochimica et Cosmochimica Acta*, v. 57, p. 303–316, doi: 10.1016/0016-  
1263 7037(93)90433-W.  
1264
- 1265 Ingall E. D. and Jahnke R. A., 1997, Influence of water- column anoxia on the elemental  
1266 fractionation of carbon and phosphorus during sediment diagenesis: *Marine Geology*, v.  
1267 139, p. 219–229, doi: 10.1016/S0025-3227(96)00112-0.  
1268
- 1269 Jilbert, T., and Slomp, C.P., 2013, Iron and manganese shuttles control the formation of  
1270 authigenic phosphorus minerals in the euxinic basins of the Baltic Sea: *Geochimica et*  
1271 *Cosmochimica Acta*, v. 107, p. 155-169, doi: 10.1016/j.gca.2013.01.005.  
1272
- 1273 Jilbert, T., Slomp, C.P., Gustafsson, B.G., and Boer, W., 2011, Beyond the Fe-P-redox  
1274 connection: preferential regeneration of phosphorus from organic matter as a key control  
1275 on Baltic Sea nutrient cycles: *Biogeosciences*, v. 8, p. 1699-1720, doi: 10.5194/bg-8-  
1276 1699-2011.  
1277

1278 Johnston, D.T., Poulton, S.W., Dehler, C., Porter, S., Husson, J., Canfield, D.E., and  
1279 Knoll, A.H., 2010, An emerging picture of Neoproterozoic ocean chemistry: Insights  
1280 from the Chuar Group, Grand Canyon, USA: *Earth and Planetary Science Letters*, v. 290,  
1281 p. 64-73, doi: 10.1016/j.epsl.2009.11.059.

1282  
1283 Kappler, A., and Newman, D.K., 2004, Formation of Fe(III)-minerals by Fe(II)-  
1284 oxidizing photoautotrophic bacteria: *Geochimica et Cosmochimica Acta*, v. 68, p. 1217–  
1285 1226, doi:10.1016/j.gca.2003.09.006.

1286 Kazakov, A.V., 1937, The phosphate facies: Origin of phosphorites and geological  
1287 factors of deposit formation: *Proceedings of the Scientific Institute of Fertilizers and*  
1288 *Insectofungicides*, v. 145, p. 1–106.

1289  
1290 Konhauser, K.O., 2007, *Introduction to Geomicrobiology*: Oxford, Blackwell Science,  
1291 425 p.

1292  
1293 Konhauser, K.O., Lalonde, S.V., Amskold, L., and Holland, H.D., 2007, Was There  
1294 Really an Archean Phosphate Crisis?: *Science*, v. 315, p. 1234, doi:  
1295 10.1126/science.1136328.

1296 Kouchinsky, A., Bengtson, S., Runnegar, B., Skovsted, C., Steiner, M., and Vendrasco,  
1297 M., 2012, Chronology of early Cambrian biomineralization: *Geological Magazine*, v.  
1298 149, p. 221-251, doi: 10.1017/S0016756811000720.

1299  
1300 Krom, M.D., and Berner, R.A., 1981, The diagenesis of phosphorus in a nearshore  
1301 marine sediment: *Geochimica et Cosmochimica Acta*, v. 45, p. 207–216, doi:  
1302 10.1016/0016-7037(81)90164-2.

1303  
1304 Laurie, J.R., 2004a, Early Middle Cambrian trilobites from Pacific Oil & Gas Baldwin 1  
1305 well, southern Georgina Basin, Northern Territory: *Memoirs of the Association of*  
1306 *Australasian Palaeontologists* v. 32, p. 127-204.

1307  
1308 Laurie, J.R., 2004b, Early Middle Cambrian trilobite faunas from NTGS Elkedra 3  
1309 corehole, southern Georgina Basin, Northern Territory: *Memoirs of the Association of*  
1310 *Australasian Palaeontologists*, v. 30, p. 221-260.

1311  
1312 Lindsay, J.F., 2002, Supersequences, superbasins, supercontinents – evidence from the  
1313 Neoproterozoic–Early Palaeozoic basins of central Australia: *Basin Research*, v. 14, p.  
1314 207-223, doi: 10.1046/j.1365-2117.2002.00170.x.

1315  
1316 Lindsay, J.F., Kruse, P.D., Green, O.R., Hawkins, E., Brasier, M.D., Cartlidge, J., and  
1317 Corfield, R.M., 2005, The Neoproterozoic–Cambrian record in Australia: a stable isotope  
1318 study: *Precambrian Research*, v. 143, p. 113–133, doi: 10.1016/j.precamres.2005.10.002.

1319  
1320 Lyons, T.W., and Severmann, S., 2006, A critical look at iron paleoredox proxies: New  
1321 insights from modern euxinic marine basins: *Geochimica et Cosmochimica Acta*, v. 70,  
1322 p. 5698–5722, doi: 10.1016/j.gca.2006.08.021.

1323  
1324 Martin, J.-M., and Meybeck, M., 1979, Elemental mass-balance of material carried by  
1325 major world rivers: *Marine Chemistry*, v. 7. P. 173-206, doi:10.1016/0304-  
1326 4203(79)90039-2.  
1327  
1328 März, C., Poulton, S.W., Beckmann, B., Küster, K., Wagner, T., and Kasten, S., 2008,  
1329 Redox sensitivity of P cycling during marine black shale formation: Dynamics of sulfidic  
1330 and anoxic, non-sulfidic bottom waters: *Geochimica et Cosmochimica Acta*, v. 72, p.  
1331 3703–3717, doi: 10.1016/j.gca.2008.04.025.  
1332  
1333 Mayer, T.D., and Jarrell, W.M., 2000, Phosphorus sorption during iron(III) oxidation in  
1334 the presence of dissolved silica: *Water Research*, v. 34, p. 3949-3956,  
1335 doi:10.1016/S0043-1354(00)00158-5.  
1336  
1337 Olivarez, A.M., and Owen, R.M., 1989, REE/Fe variations in hydrothermal sediments:  
1338 Implications for the REE content of seawater: *Geochimica et Cosmochimica Acta*, v. 53,  
1339 p. 757–762, doi:10.1016/0016-7037(89)90019-7.  
  
1340 Papineau, D., 2010, Global biogeochemical changes at both ends of the Proterozoic:  
1341 Insights from phosphorites: *Astrobiology*, v. 10, p. 165–181, doi:10.1089/ast.2009.0360.  
1342  
1343 Peng, Shanchi, and Babcock, L.E., 2011, Continuing progress on chronostratigraphic  
1344 subdivision of the Cambrian System: *Bulletin of Geosciences*, doi:  
1345 10.3140/bull.geosci.1273.  
1346  
1347 Planavsky, N.J., Rouxel, O.J., Bekker, A., Lalonde, S.V., Konhauser, K.O., Reinhard,  
1348 C.T., and Lyons, T.W., 2010, The evolution of the marine phosphate reservoir: *Nature*, v.  
1349 467, p. 1088–1090, doi:10.1038/nature09485  
1350  
1351 Porter, S.M., 2004a, Halkieriids in Middle Cambrian phosphatic limestones from  
1352 Australia: *Journal of Paleontology*, v. 78, p. 574–590, doi: 10.1666/0022-3360(2004)  
1353 078<0574:HIMCPL>2.0.CO;2.  
1354  
1355 Porter, S.M., 2004b, Closing the phosphatization window: testing for the influence of  
1356 taphonomic megabias on the pattern of small shelly fossil decline: *Palaios*, v. 19, p. 178–  
1357 183, doi: 10.1669/0883-1351(2004)019<0178.  
1358  
1359 Poulton, S.W., and Canfield, D.E., 2005, Development of a sequential extraction  
1360 procedure for iron: implications for iron partitioning in continentally derived particulates:  
1361 *Chemical Geology*, v. 214, p. 209–221, doi: 10.1016/j.chemgeo.2004.09.003.  
1362  
1363 Poulton, S.W., and Canfield, D. E., 2006, Co-diagenesis of iron and phosphorus in  
1364 hydrothermal sediments from the southern East Pacific rise: implications for the  
1365 evaluation of paleoseawater phosphate concentrations: *Geochimica et Cosmochimica*  
1366 *Acta*, v. 70, p. 5883–5898, doi: 10.1016/j.gca.2006.01.031.  
1367

1368 Poulton, S.W., and Canfield, D.E., 2011, Ferruginous Conditions: A Dominant Feature of  
1369 the Ocean through Earth's History: *Elements*, v. 7, p. 107-112,  
1370 doi:10.2113/gselements.7.2.107.  
1371

1372 Poulton S. W., and Raiswell R., 2002, The low-temperature geochemical cycle of iron:  
1373 from continental fluxes to marine sediment deposition: *American Journal of Science*, v.  
1374 302, p. 774–805, doi: 10.2475/ajs.302.9.774.  
1375

1376 Poulton S. W., Fralick, P.W., and Canfield, D.E., 2004, The transition to a sulphidic  
1377 ocean ~ 1.84 billion years ago: *Nature*, v. 431, p. 173-177, doi:10.1038/nature02912.  
1378

1379 Raiswell, R., and Berner, R.A., 1987, Organic carbon losses during burial and thermal  
1380 maturation of normal marine shales: *Geology*, v. 15, p. 853-856, doi: doi: 10.1130/0091-  
1381 7613(1987)15<853:OCLDBA>2.0.CO;2.  
1382

1383 Raiswell, R., and Canfield, D.E., 1998, Sources of iron for pyrite formation in marine  
1384 sediments: *American Journal of Science*, v. 298, p. 219–245, doi: 10.2475/ajs.298.3.219.  
1385

1386 Raiswell, R., Newton, R.J., and Wignall, P.B., 2001, An indicator of water-column  
1387 anoxia: resolution of biofacies variations in the Kimmeridge Clay (Upper Jurassic, U.K.):  
1388 *Journal of Sedimentary Research*, v. 71, p. 286–294, doi: 10.1306/070300710286.  
1389

1390 Randall, S.R., Sherman, D.M., and Vala Ragnarsdottir, K., 2001, Sorption of As(V) on  
1391 green rust (Fe<sub>4</sub>(II)Fe<sub>2</sub>(III)(OH)<sub>12</sub>SO<sub>4</sub>•3H<sub>2</sub>O) and lepidocrocite (γ-FeOOH): Surface  
1392 complexes from EXAFS spectroscopy: *Geochimica et Cosmochimica Acta*, v. 65, p.  
1393 1015–1023, doi:10.1016/S0016-7037(00)00593-7.

1394 Redfield, A.C., 1958, The biological control of chemical factors in the environment:  
1395 *American Scientist*, v. 64, p. 205-221.

1396 Riggs, S.R., 1986, Proterozoic and Cambrian phosphorites – specialist studies:  
1397 phosphogenesis and its relationship to exploration for Proterozoic and Cambrian  
1398 phosphorites: in Cook, P.J., and Shergold, J.H., eds., *Phosphate deposits of the world:  
1399 Proterozoic and Cambrian phosphorites*, Volume 1: Cambridge, UK, Cambridge  
1400 University Press, p. 352-368.  
1401

1402 Ruttenger, K.C., 1992, Development of a sequential extraction method for different  
1403 forms of phosphorus in marine sediments: *Limnology and Oceanography*, v. 37, p. 1460–  
1404 1482, doi: 10.4319/lo.1992.37.7.1460.  
1405

1406 Ruttenger, K.C., and Berner, R.A., 1993, Authigenic apatite formation and burial in  
1407 sediments from non-upwelling, continental margin environments: *Geochimica et  
1408 Cosmochimica Acta*, v. 57, p. 991-1007.  
1409

1410 Saltzman, M.R., 2005, Phosphorus, nitrogen, and the redox evolution of the Paleozoic  
1411 oceans: *Geology* v. 33, p. 573–576, doi: 10.1130/G21535.1.  
1412

1413 Schrag, D.P., Higgins, J.A., Macdonald, F.A., and Johnston, D.T., 2013, Authigenic  
1414 carbonate and the history of the global carbon cycle: *Science*, v. 339, p. 540-543, doi:  
1415 10.1126/science.1229578.  
1416

1417 Schuffert, J.D., Jahnke, R.A., Kastner, M., Leather, J., Sturz, A., and Wing, M.R., 1994,  
1418 Rates of formation of modern phosphorite off western Mexico: *Geochimica et*  
1419 *Cosmochimica Acta*, v. 58, p. 5001–5010, doi: 10.1016/0016-7037(94)90227-5.  
1420

1421 Schuffert, J.D., Kastner, M., and Jahnke, R.A., 1998, Carbon and phosphorus burial  
1422 associated with modern phosphorite formation: *Marine Geology*, v. 146, p. 21-31.  
1423

1424 Scranton, M.I., McIntyre, M., Astor, Y., Taylor, G.T., Mueller-Karger, F., and Fanning.,  
1425 K., 2006, Temporal variability in the nutrient chemistry of the Cariaco Basin: in: Neretin,  
1426 L.N. (ed.), *Past and Present Water Column Anoxia*: Springer Berlin Heidelberg New  
1427 York, p. 139-160.  
1428

1429 Severmann, S., Lyons, T.W., Anbar, A., McManus, J., and Gordon, G., 2008, Modern  
1430 iron isotope perspective on the benthic iron shuttle and the redox evolution of ancient  
1431 oceans: *Geology*, v. 36, p. 487-490, doi: 10.1130/G24670A.1.  
1432

1433 Severmann, S., McManus, J., Berelson, W.M., and Hammond, D.E., 2010, The  
1434 continental shelf benthic iron flux and its isotopic composition: *Geochimica et*  
1435 *Cosmochimica Acta*, v. 74, p. 3984-4004, doi: 10.1016/j.gca.2010.04.022.  
1436

1437 Shaffer, G., 1986, Phosphate pumps and shuttles in the Black Sea: *Nature*, v. 321, p. 515-  
1438 517, doi:10.1038/321515a0.  
1439

1440 Shemesh, A., 1990, Crystallinity and diagenesis of sedimentary apatites: *Geochimica et*  
1441 *Cosmochimica Acta*, v. 54, p. 2433-2438, doi: 10.1016/0016-7037(90)90230-I.  
1442

1443 Shen, Y., Schidlowski, M., and Chu, X., 2000, Biogeochemical approach to  
1444 understanding phosphogenic events of the terminal Proterozoic to Cambrian:  
1445 *Palaeogeography Palaeoclimatology Palaeoecology*, v. 158, p. 99–108, doi:  
1446 10.1016/S0031-0182(00)00033-X.  
1447

1448 Siever, R., 1992, The silica cycle in the Precambrian: *Geochimica et Cosmochimica Acta*,  
1449 v. 56, p. 3265-3272, doi: 10.1016/0016-7037(92)90303-Z.  
1450

1451 Slomp, C.P., Epping, E.H.G., Helder, W., and Van Raaphorst, W., 1996, A key role for  
1452 iron-bound phosphorus in authigenic apatite formation in North Atlantic continental  
1453 platform sediments: *Journal of Marine Research*, v. 54, p. 1179-1205, doi:  
1454 10.1357/0022240963213745.  
1455

1456 Slomp C. P., Thomson J., and De Lange G. J., 2004, Controls on phosphorus  
1457 regeneration and burial during formation of eastern Mediterranean sapropels: *Marine*  
1458 *Geology*, v. 203, p. 141–159, doi: 10.1016/S0025-3227(03)00335-9.



1459

1460 Southgate, P.N., 1988, A model for the development of phosphatic and calcareous  
 1461 lithofacies in the Middle Cambrian Thornton Limestone, northeast Georgina Basin,  
 1462 Australia: *Australian Journal of Earth Sciences*, v. 35, p. 111-130, doi:  
 1463 10.1080/08120098808729443.

1464

1465 Southgate, P.N., and Shergold, J.H., 1991, Application of sequence stratigraphic concepts  
 1466 to Middle Cambrian phosphogenesis, Georgina Basin, Australia: *Journal of Australian  
 1467 Geology and Geophysics*, v. 12, p. 119–144.

1468

1469 Strickland, J.D.H., and Parsons, T.R., 1972, *A Practical Handbook of Seawater Analysis:*  
 1470 *Fish Research Board of Canada.*

1471

1472 Swanson-Hysell, N.L, Rose, C.V., Calmet, C.C., Halverson, G.P., Hurtgen, M.T., and  
 1473 Maloof, A.C., 2010, Cryogenian glaciation and the onset of carbon-isotope decoupling:  
 1474 *Science*, v. 328, 608-611, doi:10.1126/science.1184508.

1475

1476 Trappe, J., 2001, A nomenclature system for granular phosphate rocks according to  
 1477 depositional texture: *Sedimentary Geology*, v. 145, p. 135–150, doi: 10.1016/S0037-  
 0738(01)00103-8.

1478

1479 Trefry, J.H., and Metz, S., 1989, Role of hydrothermal precipitates in the geochemical  
 cycling of vanadium: *Nature*, v. 342, p. 531–533, doi:10.1038/342531a0.

1480

1481 Trocine, R.P., and Trefry, J.H., 1988, Distribution and chemistry of suspended particles  
 1482 from an active hydrothermal vent site on the Mid-Atlantic Ridge at 26°N: *Earth and  
 Planetary Science Letters*, v. 88, p. 1–15, doi:10.1016/0012-821X(88)90041-6.

1483

1484 Tyrrell, T., 1999, The relative influences of nitrogen and phosphorus on oceanic primary  
 production: *Nature* v. 400, p.525–531, doi:10.1038/22941.

1485

1486 Van Cappellen, P., and Ingall, E.D., 1996, Redox stabilization of the atmosphere and  
 1487 oceans by phosphorus-limited marine productivity: *Science*, v. 271, p. 493-496, doi:  
 10.1126/science.271.5248.493.

1488

1489 Vine, J.D., and Tourtelot, E.B., 1970, Geochemistry of black shale deposits; a summary  
 1490 report: *Economic Geology*, v. 65 no. 3 p. 253-272, doi: 10.2113/gsecongeo.65.3.253.

1491

1492 Walter, M.R., Veevers, J.J., Calver, C.R., and Grey, K., 1995, Neoproterozoic  
 1493 stratigraphy of the Centralia Superbasin, Australia: *Precambrian Research*, v. 73, p. 173-  
 1494 195, doi: 10.1016/0301.9268(94)00077-5.

1495

1496 Wang, X., Hu, W., Yao, S., Chen, Q., and Xie, X., 2011, Carbon and strontium isotopes  
 1497 and global correlation of Cambrian Series 2-Series 3 carbonate rocks in the Keping area  
 1498 of the northwestern Tarim Basin, NW China: *Marine and Petroleum Geology*, v. 28, p.  
 1499 992-1002, doi:10.1016/j.marpetgeo.2011.01.006.

1500

- 1501 Xiao, S. H. and Knoll, A. H., 1999, Fossil preservation in the Neoproterozoic  
1502 Doushantuo phosphorite Lagerstatte, South China: *Lethaia*, v. 32, p. 219 – 240, doi:10.  
1503 1111/j.1502-3931.1999.tb00541.x
- 1504  
1505 Xiao, S.H., and Knoll, A.H., 2000, Phosphatized animal embryos from the  
1506 Neoproterozoic Doushantuo formation at Weng'an, Guizhou, south China: *Journal of*  
1507 *Paleontology* v. 74, p. 767–788, doi:10.1666/0022-3360(2000)074,0767:PA  
1508 EFTN.2.0.CO;2.
- 1509  
1510 Zegeye, A., Bonneville, S. Benning, L.G., Sturm, A., Fowle, D.A., Jones, C. Canfield,  
1511 D.E., Ruby, C., MacLean, L.C, Nomosatryo, S., Crowe, S.A., and Poulton, S.W., 2012,  
1512 Green rust formation controls nutrient availability in a ferruginous water column:  
1513 *Geology*, v. 40, p. 599-602, doi:10.1130/G32959.1.
- 1514  
1515 Zhu, M.-Y., Zhang, J.-M., Li, G.-X., and Yang, A.-H., 2004, Evolution of C isotopes in  
1516 the Cambrian of China: implications for Cambrian subdivision and trilobite mass  
extinctions: *Geobios*, v. 37, p. 287-301, doi: 10.1016/j.geobios.2003.06.001.

1517 **Figure captions:**

1518 **Figure 1: (A)** Areal extent of the constituent basins of the Neoproterozoic Centralian  
1519 Superbasin. The black dot marks the drill locality for core NTGS 99/1 in the southern  
1520 Georgina Basin. **(B)** Chronostratigraphy and lithostratigraphic nomenclature for the  
1521 Northern Territory outcroppings of Cambrian strata within the southern Georgina Basin  
1522 (modified from Dunster et al., 2007). The symbol “(?)” reflects uncertainties in  
1523 correlating regional Australian trilobite Zones with International Cambrian System  
1524 designations.

1525

1526 **Figure 2:** Lithofacies of the Thornton Limestone and Arthur Creek Formation in NTGS  
1527 99/1. **(A)** Sandy dolostone of the lower Thornton Limestone, just above the contact  
1528 with the underlying Paleoproterozoic granite basement (~595.8 – 595.6 mcd). **(B)**  
1529 General character of the mottled-to-stylonodular, dolomitic lower Thornton Limestone  
1530 (584 – 580.5 mcd). **(C)** Characteristic meter to sub-meter scale lithologic alternations and  
1531 color variation within limestone of the middle Thornton Limestone (577.7 – 571.4  
1532 mcd). (1) Denotes black and dark gray calcimudstone; (2) denotes lighter gray  
1533 calcimudstone, wackestone and packstone; and (3) denotes limestone grainstone. Note  
1534 the general up-package coarsening and lightening, often without cyclic or predictable  
1535 variation. **(D)** Bioclastic grainstone to mudstone transition from 570.15 – 570.05 mcd  
1536 (middle Thornton Limestone; all limestone). **(E)** Appearance of the vuggy, bioclastic  
1537 dolomitic grainstone of the upper Thornton Limestone (left) and the overlying basal  
1538 ‘hot shale’ of the lower Arthur Creek Formation (right). Contact at 554.7 mcd. **(F)** The  
1539 laminated siliciclastic shale/siltstone and calcimudstone facies of the lower Arthur Creek  
1540 Formation. **(G)** Light-gray early diagenetic nodule (calcimudstone) displacing dark-gray  
1541 laminations within the lower Arthur Creek Formation at 532.8 – 532.65 mcd (arrows  
1542 mark the exterior of the nodule). **(H)** General appearance of the interbedded siliciclastic  
1543 mudstone/siltstone and calcimudstone (neomorphosed to microspar) facies of the lower  
1544 Arthur Creek Formation above ~430 mcd.

1545

1546 **Figure 3:** Photomicrographs under plane-polarized light of authigenic apatite distribution  
1547 within the middle Thornton Limestone. **(A)** A limestone packstone with apatite

1548 replacement specifically targeting the interior of conical small shelly fossil elements at  
1549 570.35 mcd. **(B)** Wholesale matrix and grain phosphatization at of a limestone at 575.17  
1550 mcd. **(C)** Dispersed, allochthonous grains of authigenic apatite within a limestone at  
1551 560.69 mcd (see text for discussion of origin).

1552

1553 **Figure 4:** Lithology and stable isotope chemostratigraphy of the Thornton Limestone  
1554 and lower Arthur Creek Formation within drill core NTGS 99/1. For all panels, data for  
1555 the lower and middle/upper Thornton Limestone are plotted in open and solid blue  
1556 circles, respectively, while data for the Arthur Creek Formation are plotted in solid red  
1557 circles. **(A)** Generalized stratigraphic column depicting the lithology of the lower, middle,  
1558 and upper Thornton Limestone and the lower Arthur Creek Formation. Lithologic  
1559 abbreviations: Siliciclastics: slts = siltstone; Carbonates: mds = mudstone; wks =  
1560 wackestone; pks = packstone; grn = grainstone. Vertical axis reflects meters core depth  
1561 from the surface. **(B)** Carbonate carbon isotopic composition (relative to V-PDB). **(C)**  
1562 Carbonate oxygen isotopic composition (relative to V-PDB). **(D)** Total organic carbon  
1563 isotopic composition (symbol size scaled to wt.% total organic carbon (TOC)). **(E)** Cross-  
1564 plot of carbonate carbon and carbonate oxygen isotopic composition. **(F)** Cross-plot of  
1565 organic carbon and carbonate carbon isotopic composition.

1566

1567 **Figure 5:** Phosphorus and iron speciation geochemistry, molar C:P ratios, and  
1568 correlations between P and other geochemical metrics within the Thornton Limestone  
1569 and Arthur Creek Formation. **(A)** The weight percent of total phosphorus (filled green  
1570 circles) and subtotal phosphorus (open green circles) for those samples whose  $P_{Fe}$   
1571 concentrations were not determined from P-speciation geochemistry. Weight percent total  
1572 Fe (open red circles) from Fe-speciation geochemistry. Note the logarithmic scale to  
1573 emphasize, in particular, the P content of the middle and upper Thornton Limestone.  
1574 **(B)** The weight percents of operationally-defined phosphorus phases as determined by  
1575 phosphorus-speciation geochemistry. Note the logarithmic scale. See text for discussion  
1576 of the operationally-defined P phases. **(C)** The weight percents of iron phases as  
1577 determined by iron-speciation geochemistry. Note the logarithmic scale. **(D)** The molar  
1578 ratio of organic carbon to total phosphorus. Grey line intersects the axis at C:P = 106:1,

1579 the canonical Redfield ratio. **(E)** Correlation between the weight percent phosphorus  
1580 within individual samples as determined from ICP-AES versus that determined by the  
1581 sequential extraction method (see Methods section). Slope of linear regression = 1.1;  $R^2 =$   
1582 0.88. **(F)** Correlation between the zirconium to aluminum ratio (ppm/%) and the  
1583 operationally-defined  $P_{xl}$  phase (see text for discussion) determined from phosphorus  
1584 speciation geochemistry. **(G)** Cross-plot of the weight percent of highly reactive iron  
1585 species ( $Fe_{HR}$ ; oxides, magnetite, pyrite, and iron carbonates) determined from iron-  
1586 speciation geochemistry versus the weight percent of total phosphorus determined from  
1587 phosphorous-speciation geochemistry.

1588

1589 **Figure 6:** Iron-speciation geochemistry. For all panels, data for the lower and  
1590 middle/upper Thornton Limestone are plotted in open and solid blue circles,  
1591 respectively, while data for the laminated facies and interbedded siliciclastic/carbonate  
1592 mudstone facies of the Arthur Creek Formation are plotted in solid and open red circles,  
1593 respectively. Data from the Arthur Creek ‘hot shale’ appear as solid red circles with a  
1594 black outline. **(A)** A cross-plot of the weight percent total iron ( $Fe_T$ ) versus the weight  
1595 percent iron within highly reactive phases ( $Fe_{HR}$ ; oxides, magnetite, pyrite, and iron  
1596 carbonates). We plot slopes of 1 and 0.38 as a reference for comparing these carbonate  
1597 data to previously published iron-speciation data, but we do not advocate interpreting  
1598 carbonate data (blue circles) within the canonical siliciclastic framework. Slope of  
1599 regressions (not plotted) reflect the percentage of the total iron residing in highly reactive  
1600 phases (lower Thornton = 57%,  $R^2$ : 0.53; middle/upper Thornton = 89%,  $R^2$ : 0.95;  
1601 laminated facies of the Arthur Creek = 53%,  $R^2$ : 0.44; interbedded siliciclastic shale /  
1602 siltstone and carbonate mudstone facies of the Arthur Creek = 26%,  $R^2$ : 0.90). **(B)** A  
1603 cross-plot of the weight percent highly reactive iron ( $Fe_{HR}$ ) versus the weight percent iron  
1604 within pyrite ( $Fe_{py}$ ). We plot slopes of 1 and 0.8 for reference (see (a)). Slope of  
1605 regressions (not plotted) reflect the percentage of the highly reactive iron residing within  
1606 pyrite (lower Thornton = 17%,  $R^2$ : 0.07; middle/upper Thornton = 64%,  $R^2$ : 0.95;  
1607 laminated facies of the Arthur Creek = 75%,  $R^2$ : 0.95; interbedded siliciclastic shale /  
1608 siltstone and carbonate mudstone facies of the Arthur Creek = 30%,  $R^2$ : 0.50). We note  
1609 that the linear regression for the ‘hot shale’ ( $Fe_{py} = 0.8*(Fe_{HR})-0.2$ ) is the same for the

1610 lower Arthur Creek laminated facies exclusive of the ‘hot shale’ data. (C) A cross-plot of  
1611 the weight percent highly reactive iron ( $Fe_{HR}$ ) versus iron carbonate ( $Fe_{carb}$ ). Slope of  
1612 regressions (not plotted) reflect the percentage of the highly reactive iron residing within  
1613 iron carbonate (lower Thornton = 82%,  $R^2$ : 0.62; middle/upper Thornton = 31%,  $R^2$ :  
1614 0.82; laminated facies of the Arthur Creek = 25%,  $R^2$ : 0.68; interbedded siliciclastic shale  
1615 / siltstone and carbonate mudstone facies of the Arthur Creek = 52%,  $R^2$ : 0.73). We note  
1616 that the linear regression for the ‘hot shale’ ( $Fe_{carb} = 0.25*(Fe_{HR})+0.15$ ) is similar for the  
1617 lower Arthur Creek laminated facies exclusive of the ‘hot shale’ data ( $Fe_{carb} =$   
1618  $0.20*(Fe_{HR})+0.15$ ).

1619

1620 **Figure 7:** Assessing the potential contribution of organic-bound and iron-bound  
1621 phosphorus (P) to authigenic apatite precipitation. For the case of organic-bound P  
1622 delivery (left), the dashed boxes depict the median estimated weight percent organic  
1623 matter (wt.%  $\hat{C}_{org}^*$ ) necessary to account for the measured wt.% sedimentary P based on  
1624 equation (1) with a Redfield ratio of 106C:1P. Dark grey boxes represent the median  
1625 wt.% total organic carbon (TOC) measured within samples. Light gray boxes represent  
1626 the corrected wt.%  $\hat{C}_{org}^*$  (see discussion leading to equation (9)). All values plotted to  
1627 scale. Organic carbon delivery can account for all of the P within the Arthur Creek  
1628 Formation. In contrast, the blank area within the dashed Thornton Limestone box  
1629 represents the amount of  $\hat{C}_{org}^*$  that would have to have been remineralized to account for  
1630 the observed sedimentary P content if it were sourced by organic-bound P alone.

1631 For the case of iron-bound P delivery (right), the dashed boxes depict the median  
1632 measured wt.%  $P_T$  within samples while the dark grey boxes represent the estimated  
1633 delivery of iron-bound P ( $\hat{P}_{Fe}^*$ ) as determined from equation (13) assuming a partition  
1634 coefficient for ferrihydrite and a seawater phosphate concentration of 5  $\mu M$  (see text for  
1635 discussion). All values plotted to scale. In this regard, and under these assumptions, the  
1636 Fe-P delivery shuttle can account for all of the P within the Arthur Creek Formation. In  
1637 contrast, only by invoking  $Fe^{2+}$  loss from the sediment column and preferential capture of  
1638 Fe-bound P within authigenic phases, could the Fe-P shuttle have contributed more  
1639 substantially ( $> \sim 10\%$ ) to the phosphatic carbonate of the Thornton Limestone.

Figure 1

[Click here to download Figure: NTGS Fig 1.pdf](#)

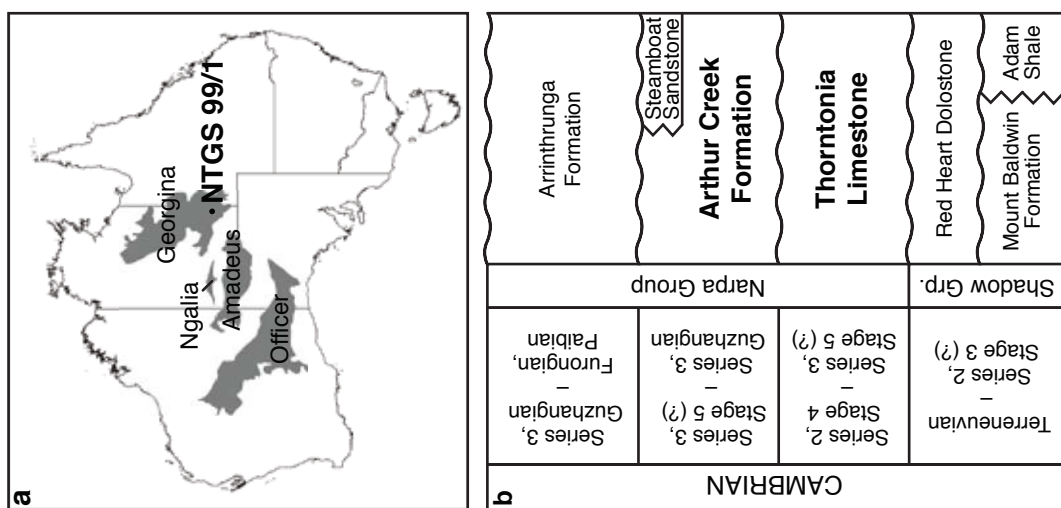


Figure 2  
Click here to download Figure: NTGS Fig 2.pdf

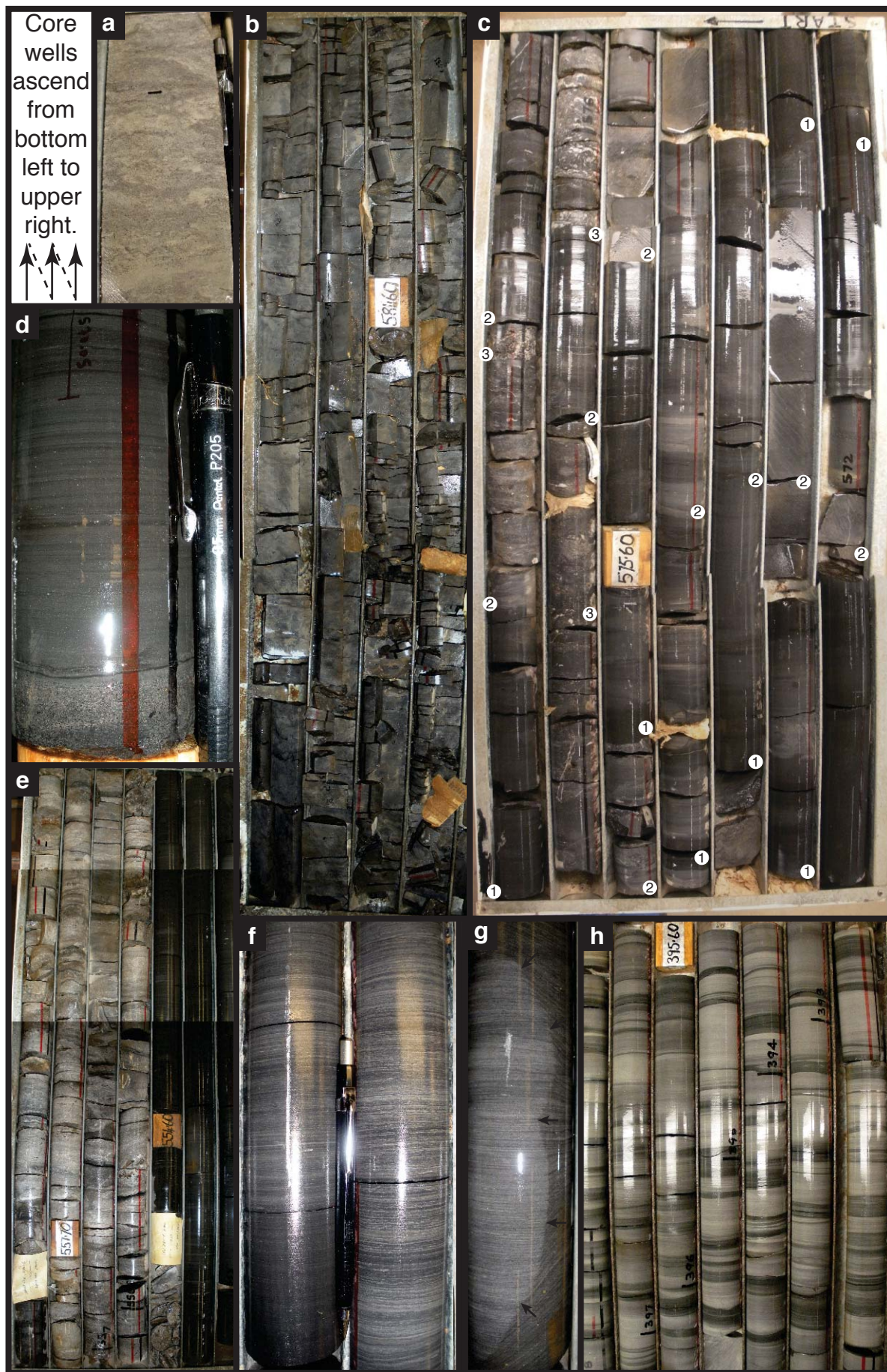




Figure 3  
[Click here to download Figure: NTGS Fig 3.pdf](#)

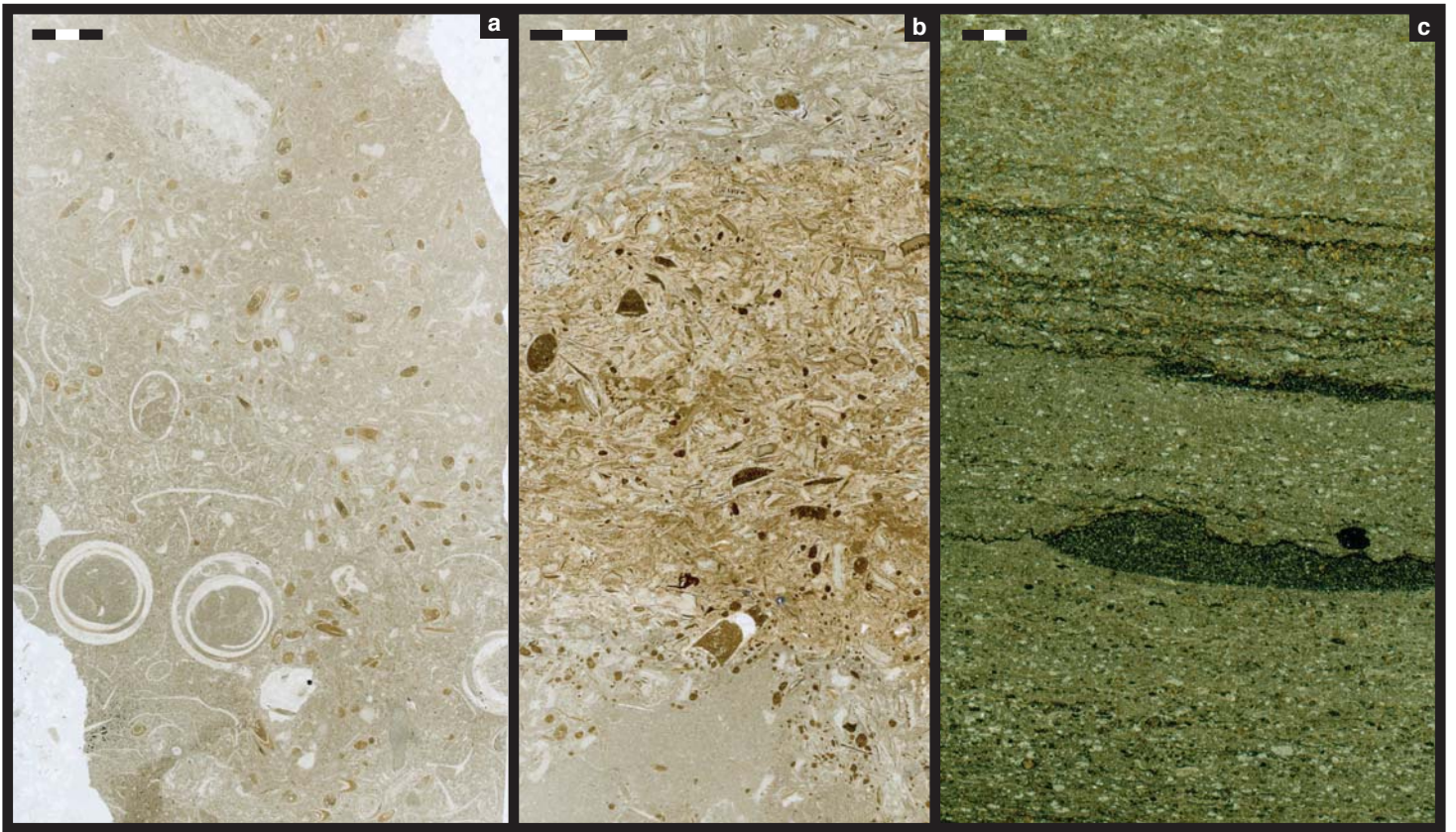


Figure 4  
[Click here to download Figure: NTGS Fig 4.pdf](#)

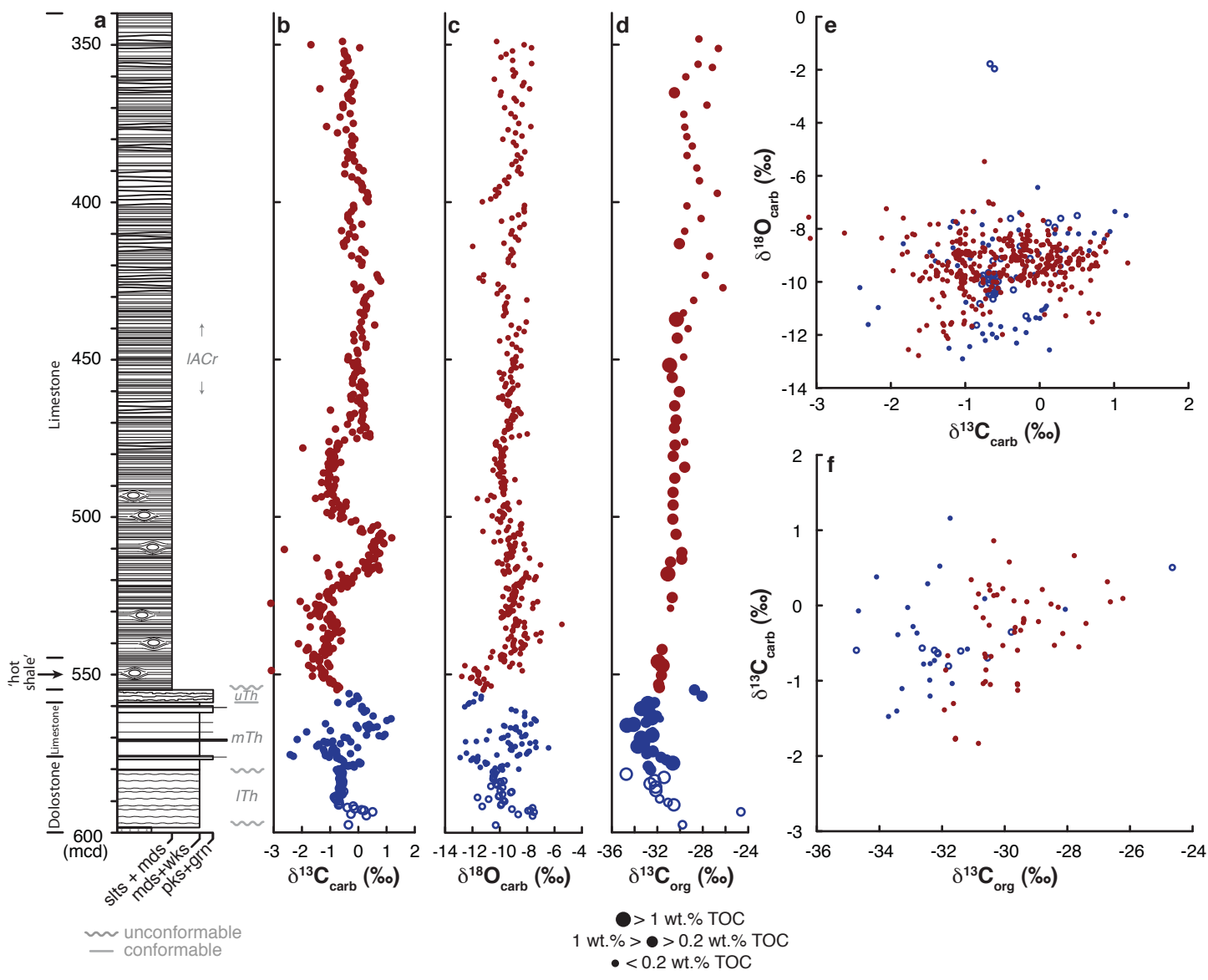


Figure 5  
[Click here to download Figure: NTGS Fig 5.pdf](#)

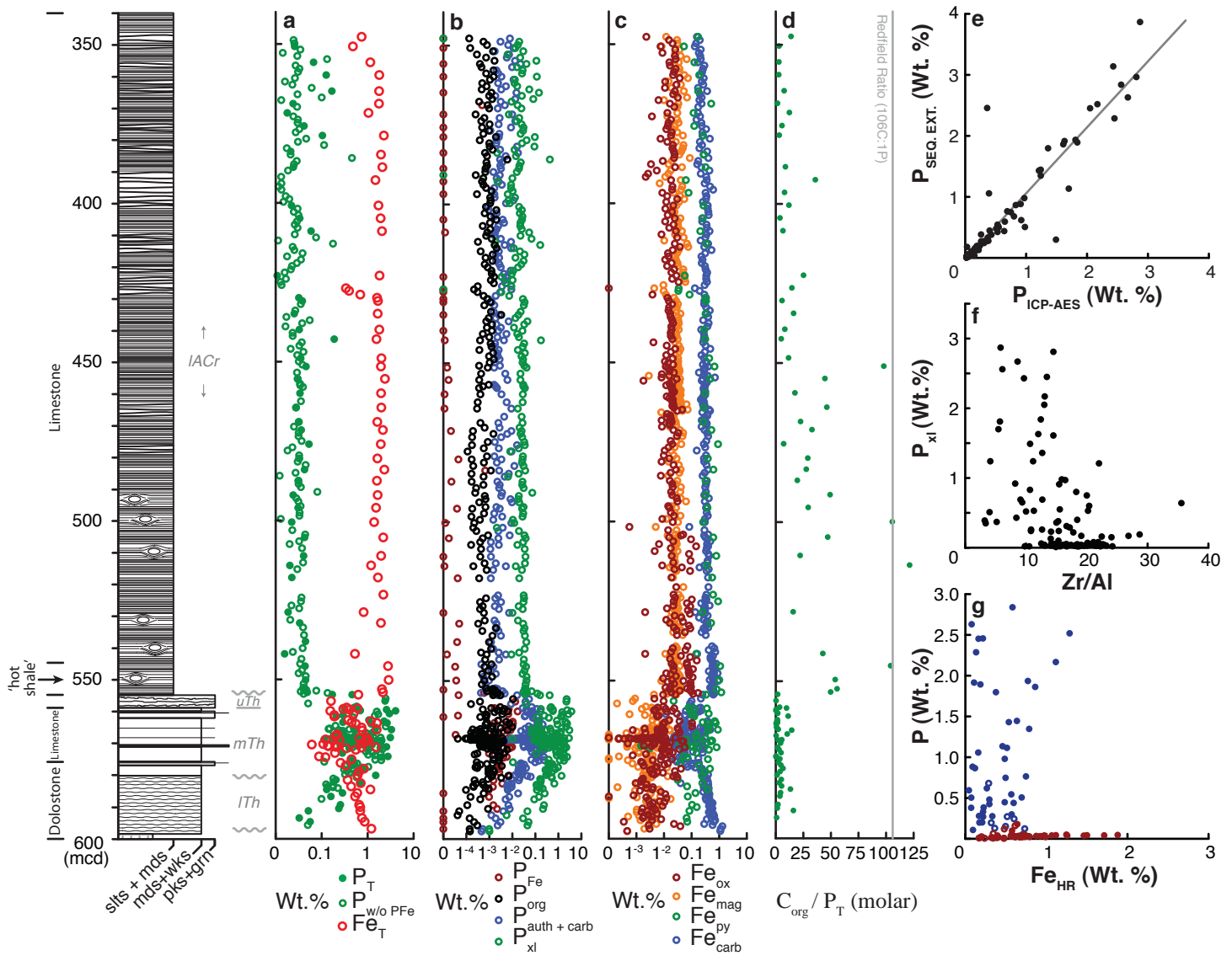


Figure 6  
[Click here to download Figure: NTGS Fig 6 revised.pdf](#)

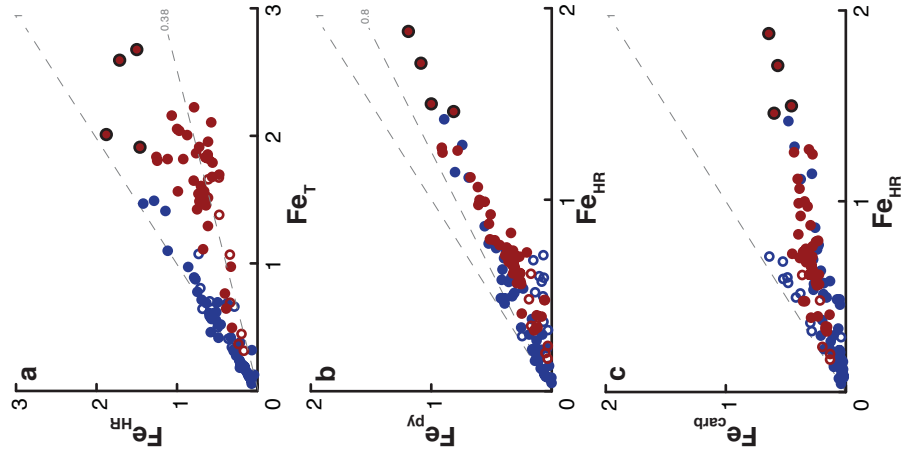
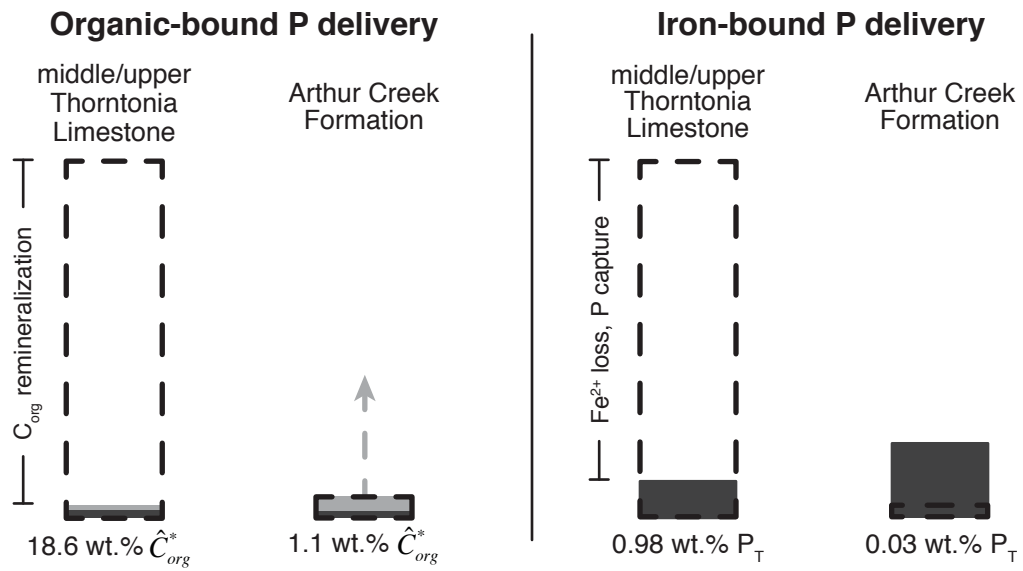


Figure 7

[Click here to download Figure: NTGS Fig 7.pdf](#)



Supplementary Information

[Click here to download Supplemental file: Supplementary Information for Revision 2.pdf](#)

Supplementary Figure 1

[Click here to download Supplemental file: NTGS Fig S1.pdf](#)

Supplementary Figure 2

[Click here to download Supplemental file: NTGS Fig S2.pdf](#)



Supplementary Data Spreadsheet

[Click here to download Supplemental file: NTGS Final Spreadsheet.xlsx](#)